





# Modelling the contributions to hyperexcitability in a mouse model of Alzheimer's disease

Martin Mittag<sup>1</sup> , Laura Mediavilla<sup>1,2,3,4</sup> , Stefan Remy<sup>5,6,7</sup>, Hermann Cuntz<sup>3,4</sup>   
and Peter Jedlicka<sup>1,3,8</sup> 

<sup>1</sup>ICAR3R – Interdisciplinary Centre for 3Rs in Animal Research, Justus Liebig University Giessen, Giessen, Germany

<sup>2</sup>School of Physiology, Pharmacology and Neuroscience, University of Bristol, Bristol, UK

<sup>3</sup>Frankfurt Institute for Advanced Studies, Frankfurt am Main, Germany

<sup>4</sup>Ernst Strüngmann Institute (ESI) for Neuroscience in cooperation with the Max Planck Society, Frankfurt am Main, Germany

<sup>5</sup>Leibniz Institute for Neurobiology, Magdeburg, Germany

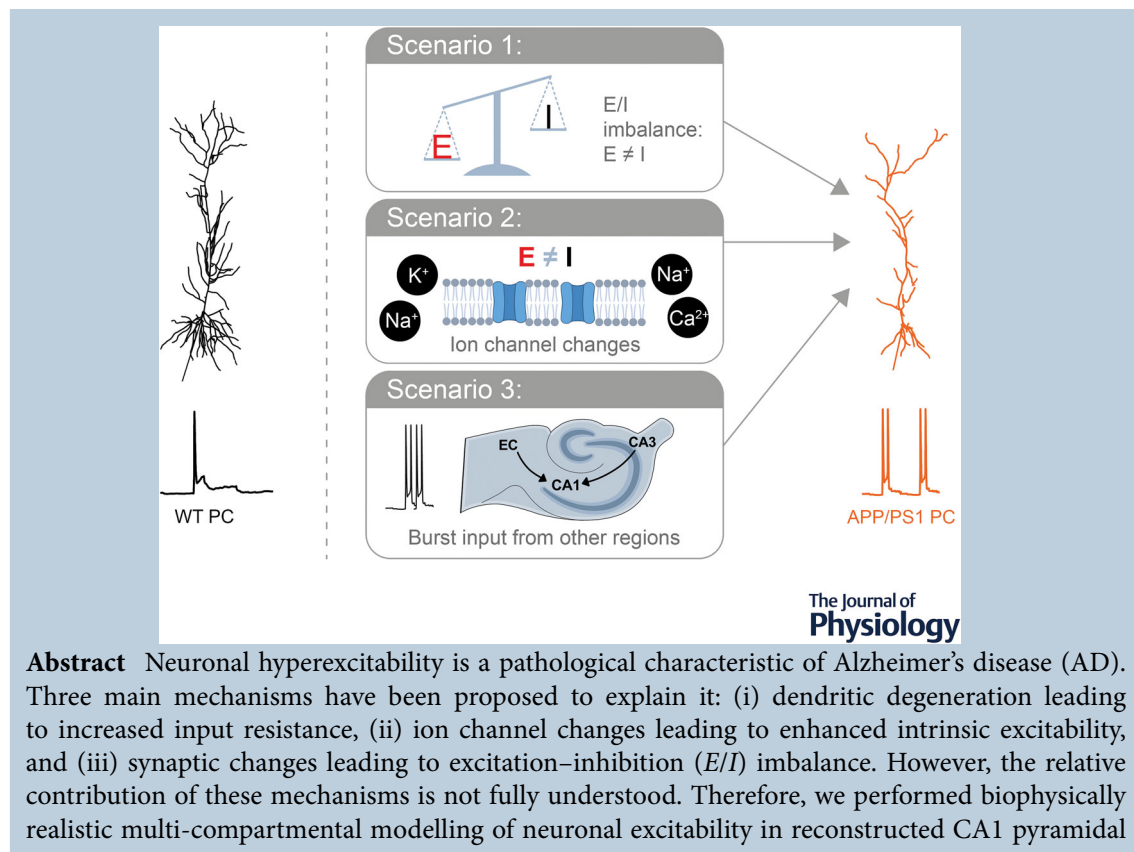
<sup>6</sup>German Center for Neurodegenerative Diseases, Magdeburg, Germany

<sup>7</sup>Center for Behavioral Brain Sciences (CBBS), Magdeburg, Germany

<sup>8</sup>Institute of Clinical Neuroanatomy, Neuroscience Center, Goethe University, Frankfurt am Main, Germany

Handling Editors: Katalin Toth & Jean-Claude Béïque

The peer review history is available in the Supporting information section of this article (<https://doi.org/10.1113/JP283401#support-information-section>).



**Abstract** Neuronal hyperexcitability is a pathological characteristic of Alzheimer's disease (AD). Three main mechanisms have been proposed to explain it: (i) dendritic degeneration leading to increased input resistance, (ii) ion channel changes leading to enhanced intrinsic excitability, and (iii) synaptic changes leading to excitation–inhibition (*E/I*) imbalance. However, the relative contribution of these mechanisms is not fully understood. Therefore, we performed biophysically realistic multi-compartmental modelling of neuronal excitability in reconstructed CA1 pyramidal

M. Mittag and L. Mediavilla are joint first authors.

H. Cuntz and P. Jedlicka are joint senior authors.

This article was first published as a preprint. Mittag M, Mediavilla L, Remy S, Cuntz H, Jedlicka P. 2022. Modelling the contributions to hyperexcitability in a mouse model of Alzheimer's disease. bioRxiv. <https://doi.org/10.1101/2022.06.29.494500>

neurons from wild-type and APP/PS1 mice, a well-established animal model of AD. We show that, for synaptic activation, the excitability-promoting effects of dendritic degeneration are cancelled out by decreased excitation due to synaptic loss. We find an interesting balance between excitability regulation and an enhanced degeneration in the basal dendrites of APP/PS1 cells, potentially leading to increased excitation by the apical but decreased excitation by the basal Schaffer collateral pathway. Furthermore, our simulations reveal three pathomechanistic scenarios that can account for the experimentally observed increase in firing and bursting of CA1 pyramidal neurons in APP/PS1 mice: scenario 1: enhanced  $E/I$  ratio; scenario 2: alteration of intrinsic ion channels ( $I_{\text{AHP}}$  down-regulated;  $I_{\text{Nap}}$ ,  $I_{\text{Na}}$  and  $I_{\text{CaT}}$  up-regulated) in addition to enhanced  $E/I$  ratio; and scenario 3: increased excitatory burst input. Our work supports the hypothesis that pathological network and ion channel changes are major contributors to neuronal hyperexcitability in AD. Overall, our results are in line with the concept of multi-causality according to which multiple different disruptions are separately sufficient but no single particular disruption is necessary for neuronal hyperexcitability.

(Received 30 June 2022; accepted after revision 24 January 2023; first published online 3 February 2023)

**Corresponding author** M. Mittag and L. Mediavilla: ICAR3R – Interdisciplinary Centre for 3Rs in Animal Research, Justus Liebig University Giessen, 35390 Giessen, Germany. Email: martin.mittag@informatik.med.uni-giessen.de and laura.medivillasantos@bristol.ac.uk

**Abstract figure legend** Three scenarios of extrinsic and intrinsic mechanisms can explain hyperexcitability of APP/PS1 model pyramidal cells (PCs). Using a computational model, we find that changes in the extrinsic network and intrinsic biophysical neuronal properties rather than dendritic degeneration alone explain the altered firing behaviour (i.e. increased firing rates and transition to bursting) observed in Alzheimer's disease (AD).

### Key points

- This work presents simulations of synaptically driven responses in pyramidal cells (PCs) with Alzheimer's disease (AD)-related dendritic degeneration.
- Dendritic degeneration alone alters PC responses to layer-specific input but additional pathomechanistic scenarios are required to explain neuronal hyperexcitability in AD as follows.
- Possible scenario 1: AD-related increased excitatory input together with decreased inhibitory input ( $E/I$  imbalance) can lead to hyperexcitability in PCs.
- Possible scenario 2: changes in  $E/I$  balance combined with altered ion channel properties can account for hyperexcitability in AD.
- Possible scenario 3: burst hyperactivity of the surrounding network can explain hyperexcitability of PCs during AD.

## Introduction

Neuronal hyperexcitability has been described as a characteristic feature of Alzheimer's disease (AD; Kazim

et al., 2021; Palop & Mucke, 2009; Targa Dias Anastacio et al., 2022; Vossel et al., 2017; Zott et al., 2018). It is observed in the early phases of the disease progression

**Martin Mittag** received his master's degree in physics at the Radboud University of Nijmegen, the Netherlands, focusing on artificial neural networks and stochastic optimal control. He joined the Interdisciplinary Centre for 3Rs in Animal Research, Justus Liebig University Giessen, Germany, in 2017 to work on his PhD in computational neuroscience. There, he studies the impact of dendritic morphology and biophysics on neuronal excitability using compartmental modelling of single cells. **Laura Mediavilla** is a PhD student in Neural Dynamics at the University of Bristol, UK. She received her master's degree in Interdisciplinary Neuroscience from Frankfurt University in 2018, where she studied the interplay between dendritic structural degeneration observed in Alzheimer's disease and the input-to-output function of a cell using compartmental models. Her current research focuses on studying the cortex-wide dynamics of neuronal populations across early brain development.



(Busche & Konnerth, 2015; Dickerson et al., 2005) at the circuit as well as single cell level. Observations of hyperexcitability in AD patients (Horvath et al., 2021; Palop & Mucke, 2016; Palop et al., 2007; Ranasinghe et al., 2022; Vossel et al., 2013, 2016, 2021) are consistent with data from mouse models of AD (Busche et al., 2008, 2012; Busche, Grienberger et al., 2015; Busche, Kekuš et al., 2015; Grienberger et al., 2012; Hall et al., 2015; Keskin et al., 2017; Liebscher et al., 2016; Maier et al., 2014; Müller et al., 2021; Rudinskiy et al., 2012; Šišková et al., 2014; Scala et al., 2015; Xu et al., 2015). Most studies showing AD-associated hyperactivity such as increased frequency of calcium transients or the occurrence of hyperactive neuron populations in mice (Busche & Konnerth, 2015; Busche et al., 2008, 2012) and rats (Sosulina et al., 2021) and increased seizure activity during electroencephalographic (EEG) recordings in the mouse hippocampus (Palop & Mucke, 2009; Palop et al., 2007) do not or cannot determine if the mode of increased neuronal excitability comes from an enhanced single spike rate or from a switch to enhanced burst firing. However, the change of firing mode towards stronger burst firing is a feature in several neurological disorders such

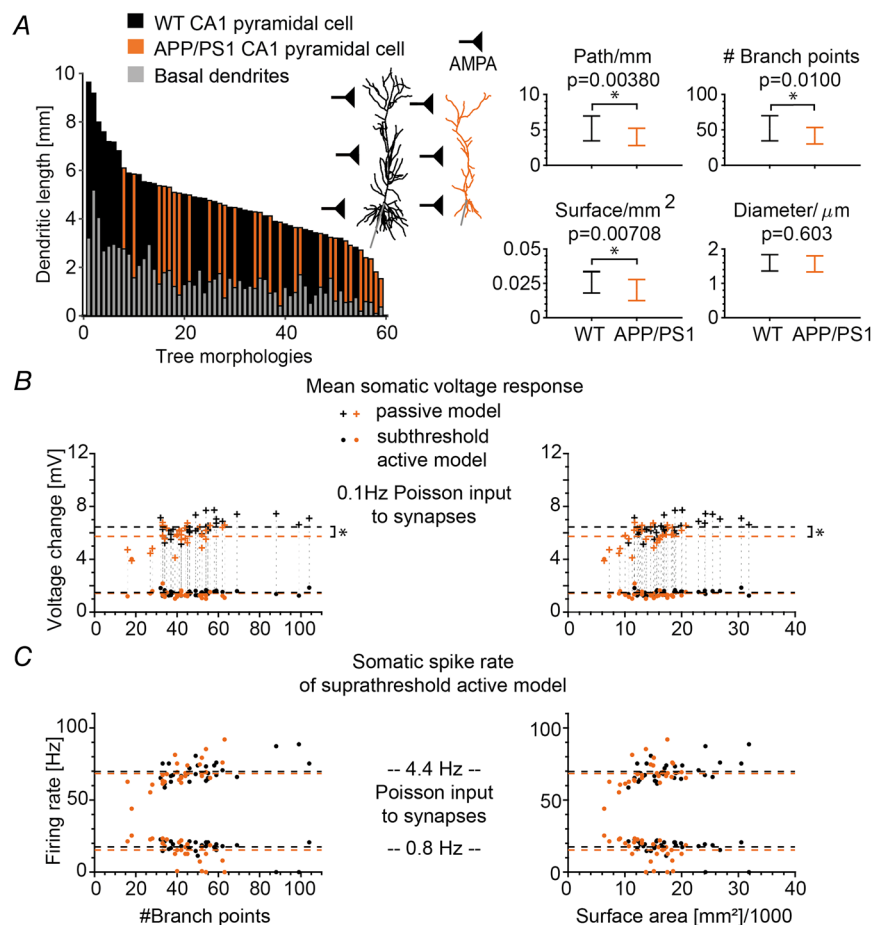
as epilepsy (Pothmann et al., 2019; Sanabria et al., 2001; Wellmer et al., 2002) and chronic stress (Okuhara & Beck, 1998). In AD, amyloid- $\beta$  accumulation has been linked to a change in burst firing pattern (Chen, 2005; Kellner et al., 2014; Minkeviciene et al., 2009). For example in APP/PS1 model mice, *in vivo* and *in vitro* patch-clamp and *in vivo* extracellular recordings revealed hyperactivity of CA1 pyramidal neurons in the form of increased mean firing rate as well as enhanced bursting (Šišková et al., 2014). In this study, we specifically aim to reproduce the data of figure 1B of Šišková et al. (2014) and generally show possible mechanisms of hyperexcitability.

Three prominent explanations of neuronal hyperexcitability in AD (including the enhanced bursting) have been proposed (Ferraio Santos et al., 2010; Maestú et al., 2021; Targa Dias Anastacio et al., 2022; Vyas et al., 2020; Zott et al., 2018), which will be introduced in detail below: alterations of intrinsic properties by (i) dendritic degeneration, (ii) ion channel changes, or (iii) alterations of extrinsic network properties by enhanced synaptic excitation/inhibition (*E/I*) ratio.

With regard to the first explanation, atrophic degeneration of neuronal dendrites is one of the hallmarks

**Figure 1. Overview of morphological measures for reconstructed WT and APP/PS1 CA1 pyramidal cells and their influence on responses to distributed synaptic inputs**

A, left, sorted distribution of the dendritic length of all cells shown, ranked from longest to shortest. Black denotes the WT cell, orange the APP/PS1 cell and grey is the basal portion of the total dendritic length. Right, the comparison of average dendritic path length, number of branching points and dendrite surface area shows significant differences depicted by the asterisks. The average dendritic diameter was similar in both cell groups. B, voltage change responses of passive and subthreshold active cells to distributed AMPA inputs as in Results but plotted against the number of branch points (left) and the surface area (right). The dashed lines show the mean activity of the WT (black) and APP/PS1 (orange) CA1 cell groups. The asterisk depicts  $P = 0.000467$ . C, firing rate responses to active distributed AMPA inputs plotted against the number of branch points (left) and the surface area (right). The dashed lines show the mean firing rates per group. [Colour figure can be viewed at [wileyonlinelibrary.com](http://wileyonlinelibrary.com)]



of AD (Anderton et al., 1998; Braak & Braak, 1991; Braak et al., 1993), well documented both in patients (Augustinack et al., 2002; Grutzendler et al., 2007; Merino-Serrais et al., 2013) and in animal models (Grutzendler et al., 2007; Le et al., 2001; Moolman et al., 2004; Tsai et al., 2004). It progressively affects brain areas that play important roles in learning and memory, such as the dentate gyrus, the CA1 and the subiculum area of the hippocampus and cerebral cortex (Adlard & Vickers, 2002; Falke et al., 2003; Geula et al., 1998; Grutzendler et al., 2007; Spires & Hyman, 2004). Dendritic changes have been suggested to play a major role in the pathogenesis of AD (Cochran et al., 2014). However, the functional consequences of dendritic degeneration associated with a concurrent synapse loss (Masliah et al., 1994), which is another hallmark of AD (Terry et al., 1991), have only recently begun to be elucidated in APP/PS1 mice (Šišková et al., 2014). The dendritic degeneration in CA1 pyramidal cells (PCs) has been proposed to contribute to their hyperexcitability in the form of higher firing rates associated with enhanced bursting (Šišková et al., 2014). However, if also synaptic loss is considered then dendritic degeneration with its decrease in input conductance might counteract the lower number of synapses, homeostatically maintaining normal excitability (Cuntz et al., 2021; Platschek et al., 2016, 2017). To explore this possibility, we implemented both synapse loss and dendritic degeneration (Šišková et al., 2014) in compartmental CA1 PC models and analysed their synaptically driven activity.

With regard to the second explanation, modifications of intrinsic excitability due to changes in ionic channels have also been implicated in the pathogenesis of the AD (Kerrigan et al., 2014). Experimental studies have reported alterations in the density of several active membrane channels, such as the A-type  $K^+$  channel, voltage-dependent  $Na^+$  channel and delayed-rectifier  $K^+$  channel (Brown et al., 2011; Ghatak et al., 2019; Good et al., 1996; Kim et al., 2007; Liu et al., 2015; Scala et al., 2015; Wang et al., 2016). Several studies have provided evidence supporting the contribution of the reduced A-type  $K^+$  current to the hyperexcitability observed in AD-affected neurons (Chen, 2005; Culmone & Migliore, 2012; Frazzini et al., 2016; Morse et al., 2010; Rodrigues et al., 2017; Scala et al., 2015). Likewise, increased excitability has also been documented in a mouse model of AD, where it was attributed to changes in the dendritic tree and alterations in the expression and function of A-type  $K^+$  channels (Hall et al., 2015). There has been contradictory evidence showing the role of the hyperpolarisation-activated H-channel with studies indicating either a decrease or an increase of its density (Musial et al., 2018; Vitale et al., 2021). Further experimental findings have revealed the influence of the small and large calcium-activated  $K^+$  channels in AD

model mice (Beck & Yaari, 2008; Wang, Kang et al., 2015; Wang, Zhang et al., 2015; Zhang et al., 2014). Also the disruption of  $Ca^{2+}$  signalling and  $Ca^{2+}$  channels plays an important role in the pathogenesis of AD (Anekonda et al., 2011; Bezprozvanny & Mattson, 2008; Bojarski et al., 2008; Tan et al., 2012). For AD-related pathologies the L-type  $Ca^{2+}$  channel (Anekonda et al., 2011; Berridge, 2014), the A-type  $K^+$  channel (Chen, 2005) and  $Na^+$  channels (Ghatak et al., 2019; Müller et al., 2021; Wang et al., 2016) have been shown to be involved in burst rate amplification. Modelling studies (Garg et al., 2021; Medlock et al., 2018) confirm the role of  $Ca^{2+}$  channels for enhanced burst firing. Evidently, the modification of intrinsic excitability due to alterations in ion channel expression is well documented in AD. However, its interplay with synaptic and dendritic changes has not yet been fully clarified.

With regard to the third explanation, several studies have provided evidence for enhanced glutamatergic excitation (Busche & Konnerth, 2016; Zott et al., 2019) and impaired inhibition during AD (Ambrad Giovannetti & Fuhrmann, 2019; Busche et al., 2008, 2012; Gervais et al., 2022; Melgosa-Ecenarro et al., 2022; Palop & Mucke, 2016; Rüter et al., 2020; Schmid et al., 2016; Takahashi et al., 2010; Xu et al., 2020; but see also Hollnagel et al., 2019). This includes decreased perisomatic inhibition (Verret et al., 2012), which can alter the firing pattern towards more bursts (Pouille & Scanziani, 2004). The excitatory drive constitutes one of the main determinants of neuronal spontaneous firing rate (Frere & Slutsky, 2018). Therefore, a shift towards synaptic excitation (Roberson et al., 2011) that increases the  $E/I$  ratio may explain enhanced firing rates in AD during spontaneous activity. Epileptiform disruption of spontaneous neuronal activity in hippocampal circuits is a typical feature in mouse models of AD (Palop et al., 2007), where sharp synchronous discharges linked to memory deficits have been observed (Born et al., 2014). In line with the relevance of enhanced  $E/I$  ratio, recent clinical observations suggest that pharmacological suppression of glutamatergic excitation (by levetiracetam) is a promising way of improving cognition in AD patients with epileptiform hyperexcitability (Vossel et al., 2021). CA1 pyramidal neurons are part of a larger network and receive input from CA3 and the entorhinal cortex (EC). Previous studies have shown hyperactivity in EC for AD pathology models of mice (Angulo et al., 2017; Khan et al., 2013; Nuriel et al., 2017; Petrache et al., 2019) as well as CA3 (Kazim et al., 2017; see also computer AD models containing CA1 and CA3, Świetlik et al., 2019). An increased excitatory network activity in these pre-synaptic areas could therefore spread to CA1 and contribute to the observed hyperexcitability and burstiness in AD cells.

Although these three groups of mechanisms have been proposed to account for AD-related hyperexcitability,

their contributions and mutual interplay are not fully understood. Therefore, in the present study, we took advantage of the unique feature of biophysical modelling that enables the investigation of isolated and combined parameter changes. The computational approach allowed us to disentangle which changes and their contributions to hyperexcitability in AD are most relevant. First, we investigated whether the AD-related dendritic degeneration in APP/PS1 mice by itself supports hyperactivation of their CA1 pyramidal neurons or, alternatively, whether it compensates for the loss of synapses and helps maintain unchanged neuronal spike rates. Our biophysically detailed modelling of realistic dendrite morphologies from APP/PS1 mice indicates that the observed morphological changes alone do not lead to the hyperexcitability of CA1 pyramidal neurons for whole cell distributed synaptic inputs. Increased degeneration in the basal dendrites of APP/PS1 cells can lead to a region-dependent change in excitation as seen in clustered stimulations of main layer-specific CA1 input pathways. Second, in line with a multi-causal pathogenesis, we showed that the increased excitation of CA1 PCs can be sufficiently accounted for by a shift in  $E/I$  balance towards glutamatergic network excitation (increased network activity, especially in the form of bursts, and decreased inhibitory inputs) or by its combination with changes in ion channel expression ( $I_{AHP}$  channel density down-regulated;  $I_{NaP}$ ,  $I_{Na}$  and  $I_{CaT}$  up-regulated) leading to increased intrinsic excitability of the cells. We compared our results with the experimental data of Šišková et al. (2014), which showed a firing mode change from single spikes to bursting observed in APP/PS1 cells. Our results are largely in line with the concept of degeneracy (Edelman & Gally, 2001; Tononi et al., 1999), according to which similar physiological but also similar pathological states such as neural hyperexcitability can emerge from multiple distinct mechanisms (Kamaleddin, 2022; Medlock et al., 2022; Neymotin et al., 2016; O'Leary, 2018; Ratté & Prescott, 2016; Stöber et al., 2022).

## Methods

### Ethical approval

Neither human nor animal experiments were performed for this research paper since all investigations were done *in silico*.

### Data analysis

Morphological analysis was performed in MATLAB (version 2018a, The MathWorks Inc., Natick, MA, USA) using our own software package, the TREES toolbox (Cuntz et al., 2011; www.treestoolbox.org). All passive

and active compartmental model simulations were run in NEURON (Hines & Carnevale, 2004) via a newly developed software to control NEURON with MATLAB and the TREES toolbox, the TREES-to-NEURON (T2N) interface (Beining et al., 2017). The results and figure panels throughout the manuscript were further analysed and generated with MATLAB and Adobe Illustrator CS6.

### Dendrite morphologies

The morphology data set used in the study included 59 mouse hippocampal CA1 PC reconstructions from 10- to 14-month-old wild-type (WT;  $n = 31$ ) and APP/PS1 ( $n = 28$ ) mice (Šišková et al., 2014). Each 3D reconstruction was translated to a format supported by MATLAB and carefully examined for any morphological inconsistencies and physical integrity (see distribution of cells by length and two example morphologies in Fig. 1A, left). Pre-processing of the morphologies included therefore the removal of unrealistic nodes and trifurcations (*repair\_tree*, *clean\_tree*) and the correction of unrealistic sudden shifts especially in the  $z$ -axis (*zcorr\_tree*, *smooth\_tree*). When divided, the separated basal and apical subtrees had to be concatenated. All nodes from the reconstruction were redistributed to have equal inter-nodal distances of  $1 \mu\text{m}$  for a high structural resolution (*resample\_tree*). The dendritic diameter was tapered (quadratic taper: *quadfit\_tree*, *quaddiameter\_tree* as in Cuntz et al., 2007) in order to correct for unrealistically distributed diameters in the original reconstructions. Statistical comparison of average dendritic path length (WT  $5.19 \pm 1.75 \text{ mm}$ , APP/PS1  $4.00 \pm 1.22 \text{ mm}$ ,  $P = 0.00380$ ), number of branching points (WT  $52.16 \pm 17.79$ , APP/PS1  $41.61 \pm 11.67$ ,  $P = 0.0100$ ) and dendrite surface area (WT  $0.026 \pm 0.008 \text{ mm}^2$ , APP/PS1  $0.02 \pm 0.007 \text{ mm}^2$ ,  $P = 0.00708$ ) between WT and APP/PS1 model cell groups showed significant differences (Fig. 1A, right). Due to the morphological differences, we investigated in this study the influence of dendritic length, surface area and number of branch points on voltage change and firing rate in response to synaptic stimulation (Fig. 1B and C). The average dendritic diameter was similar in both cell groups (WT  $1.6 \pm 0.24 \mu\text{m}$ , APP/PS1  $1.57 \pm 0.23 \mu\text{m}$ ,  $P = 0.603$ ). However, PCs typically have an average dendritic diameter of  $0.8 \mu\text{m}$  (Benavides-Piccione et al., 2020). The dendrites were therefore normalised to a lower average diameter of  $1 \mu\text{m}$  as part of the morphologies pre-processing as described previously (Cuntz et al., 2021). None of the reconstructions included a soma or an axon. Therefore, an artificial cosine shaped soma was added having a surface area of  $560 \mu\text{m}^2$  ( $\sim 4 \times 137 \mu\text{m}^2$ , which is the soma perimeter) and a maximum diameter of  $10 \mu\text{m}$ , corresponding to the typical average size of

somata in pyramidal neurons (Benavides-Piccione et al., 2020). For consistency the same axon was appended to the soma of all neurons. The axon was created using several concatenated cylindrical compartments with a total length of 630  $\mu\text{m}$  and an average diameter of 0.5  $\mu\text{m}$ , modelling the axon hillock, initial segment, five nodes of Ranvier and myelination (Benavides-Piccione et al., 2020). For the simulations with artificially equalized basal/apical dendrite ratios (see Results), the original WT and APP/PS1 cell morphologies were artificially scaled in order to obtain specific basal/apical length ratios of 30/70. Each cell morphology kept its original total dendritic length, varying only the relative length proportion between the basal and the apical dendrites.

### Normalisation of laminar structure and dendritic regions

In order to evaluate the influence of morphology alone on the cell's output, the biophysical properties with electrotonic parameters and active mechanisms must be consistently distributed. Therefore, a comprehensive way to define subregions with distance boundaries was needed. To do this, we defined a normalised division of the CA1 dendrites into the different hippocampal layers and dendritic subregions. The anatomical boundaries of the CA1 hippocampal area were delimited depending on the contribution of the dendritic length to each layer (Bannister & Larkman, 1995; Megías et al., 2001; Trommald et al., 1995), making sure that, on average, the stratum oriens, stratum radiatum (SR) and stratum lacunosum-moleculare (SLM) represented 40%, 40% and 20% of the total CA1 dendritic length, respectively. Two major division planes were defined, the stratum oriens–stratum pyramidale plane that cut through the cell soma and was orthogonal to the direction of growth of the apical dendrite; and the SR–SLM boundary, which was parallel to the stratum oriens–stratum pyramidale plane layer, leaving in between both planes the relative contribution (67%) of the SR to the apical dendritic length (Fig. 2A). The CA1 PC structure was further divided into dendritic sublayers, which were used as inflexion points for changes in electrotonic properties and active channels along the somato-dendritic axis. Four distance inflexion points appear in the majority of CA1 cell models available in *ModelDB*: 100, 300, 350 and 500  $\mu\text{m}$  path length (or laminar depth). Each of these distance values was translated into dendritic apical length contribution by calculating the amount of dendritic length that lies within the different distance limits for both ion channel distribution approaches, path and perpendicular length, and expressed as percentage of apical length. We extracted these values from a large data set of CA1 rat cell morphologies available at NeuroMorpho.Org, which were

based on previous experimental studies (Bezchlibnyk et al., 2017; Carnevale et al., 1997; Golding et al., 2005; Megías et al., 2001; Pyapali et al., 1998). The dendritic apical length within each of the boundaries did not differ substantially, estimating a contribution of 8%, 48%, 67% (matches the SR–SLM boundary) and 85% of total apical length for each distance limit, respectively. The entire path

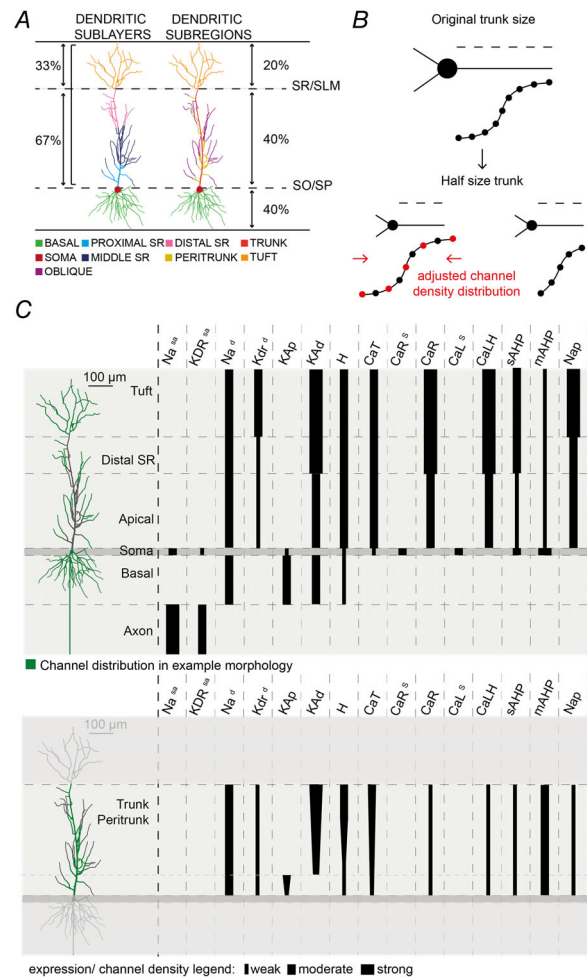


**Figure 2. Dendritic regions and ion channel distributions in reconstructed CA1 pyramidal cells adapted from the biophysical model by Poirazi et al. (2003b)**

A, dendritic layer distribution. Each subdivision represents the estimated boundary for changes in electrotonic properties and channel densities. B, schematic representation of the rescaling process for the non-linear distribution of ion channels in morphologically diverse CA1 pyramidal cell models. Top, original cell morphology's trunk laminar depth. Bottom left, cell with an apical trunk half the size of the original. The original laminar depth vector is resampled. Bottom right, the vector is then compressed to fit the new cell's trunk size. C, schematic summary of the ion channel composition of the CA1 pyramidal cell model with Poirazi biophysics (Poirazi et al., 2003b). Left, exemplary morphology. Right, distribution of ion channel density. The relative thickness of the lines indicates the channel density. SLM, stratum lacunosum-moleculare; SO, stratum oriens; SP, stratum pyramidale; SR, stratum radiatum. [Colour figure can be viewed at [wileyonlinelibrary.com](http://wileyonlinelibrary.com)]

from each terminal branch tip that invaded the SLM was drawn. Those nodes, shared by more than half of the paths that were below the SR–SLM boundary, were defined as the main apical dendrite (trunk). The nodes above the SR–SLM limit were designated as the apical tuft. The branches stemming from the trunk that failed to invade the SLM (less than 2/3 of the total branch length trespassed the SLM) were labelled as oblique dendrites.

### Biophysical properties of CA1 PC models

The determination of normalised dendritic regions in morphologies of different shapes and sizes (as described above) allowed us to design a coherent morphology-independent way of generalising existing biophysical CA1 PC models to diverse morphologies. For the main results (see below), we implemented a biophysically realistic model based on the model developed and validated by Poirazi et al. (2003a,b) (see model no. 20212 in ModelDB (Hines & Carnevale, 2004; McDougal et al., 2017) translated to T2N in Cuntz et al. (2021)). The model consisted of active and passive membrane mechanisms including 16 types of ion channels, most of them non-uniformly distributed along the somato-dendritic axis (Fig. 2C). NEURON channel models were used with no modification. The number of segments per section was defined each  $75 \mu\text{m}$ .

In order to implement the same non-uniform distribution of channel densities for different PCs whose apical trunk size can vary greatly (as well as its overall size), the original morphology's trunk laminar depth in the model by Poirazi et al. (2003b) was extracted and adjusted to fit the trunk size from each of the cells in the data set. This means a vector from 0 to a maximum distance of  $423.75 \mu\text{m}$  (maximum laminar depth of the original cell) was generated, and rescaled at different intervals that depended on the size of each new cell's apical trunk, but that kept the same minimum and maximum depth values (Fig. 2B). As the channel densities were multiplied by these distance values, every cell had the same minimum and maximum conductance value for the different channels, and kept a proportional distance dependency of conductance changes (same distribution function), when compared to the original model cell.

The dendritic region specification employed for the channel distribution in this model was based on the archetypical regions in PCs, where the cells are divided into basal, somatic, trunk, apical (oblique and tuft) and axonal regions as described in detail above and shown in Fig. 2A. In addition, the membrane properties for the oblique side branches within the first  $50 \mu\text{m}$  from the trunk were set to follow the respective trunk conductance values. This extra dendritic region was defined as the peritrunk area. Likewise, distal apical regions, defined

by the distal SR and tuft layer boundaries, also possess modified conductance densities in order to account for some specific distal changes in channel distribution. The model does not include any compensation for spines.

To test whether our main results (see Results) computed by the biophysical model of Poirazi et al. (2003b) are robust and generalisable to other biophysical models, in Fig. 3 we implemented a second model by Jarsky et al. (2005) (see model no. 116 084 in ModelDB). This model included uniform passive parameters throughout the cell and four different types of active conductances: a voltage-gated sodium conductance, a delayed-rectifier potassium conductance, and a proximal and distal A-type potassium conductance as seen in Fig. 3A. All NEURON channel models were used with no modification. The dendritic region specification employed for the channel distribution in this model was based on the dendritic sublayer division as in Fig. 2A, where the cells were divided into basal, somatic, proximal SR, middle SR, distal SR, tuft (proximal SLM and distal SLM) and axonal regions. Moreover, this model included a spine-correction mechanism that multiplies the specific membrane capacitance and divides the specific membrane resistance for regions above the distal SR by 2. The model by Jarsky et al. (2005) yielded similar results to the model by Poirazi et al. (2003b) with the APP/PS1 cells on average showing equal or lower activity compared to the WT cells (see Fig. 3C–E, mean voltage passive model: WT  $9.11 \pm 0.43 \text{ mV}$ , APP/PS1  $8.91 \pm 0.64 \text{ mV}$ ; mean voltage sub-threshold active model: WT  $1.69 \pm 0.18 \text{ mV}$ , APP/PS1  $1.53 \pm 0.22 \text{ mV}$ , the asterisk indicates  $P = 0.00360$ ; output firing rate to 6 Hz input: WT  $49.05 \pm 2.52 \text{ Hz}$ , APP/PS1  $45.12 \pm 8.9 \text{ Hz}$ ,  $P = 0.0217$ ; 15 Hz input: WT  $76.11 \pm 4.58 \text{ Hz}$ , APP/PS1  $71.66 \pm 5.07 \text{ Hz}$ ,  $P = 0.000817$ ).

### Validation and robustness of the T2N implemented models

Two models employed in this work (Jarsky et al., 2005; Poirazi et al., 2003a,b) have been previously validated and calibrated by their authors on data from published *in vitro* physiological studies. However, as we implemented these original CA1 PC models using a different computational tool (T2N; Beining et al., 2017; Cuntz et al., 2021), it was necessary to validate the implementation against the originally developed models, taking care that it did not modify the behaviour of the cell, qualitatively and quantitatively. Accordingly, several electrophysiological features were evaluated and compared between the original cell models built in NEURON and the T2N implemented versions (Table 1). However, despite the fact that the cell morphology used in the original compartmental model slightly differed from the one used in the T2N version of the model (due to the translation

of the structure from frusta (NEURON) to cylinders (TREES/T2N) and back to frusta), small variability in the electrophysiological properties fell within an acceptable range.

Additionally to the validation of the model implementation in T2N, the plausibility of both rat biophysical models was evaluated by implementing them in a broader set of rat hippocampal CA1 PC morphologies (obtained from the July 2018 version of the NeuroMorpho.org database; Ascoli et al., 2007) and comparing their electrophysiological properties with experimental values (obtained from the NeuroElectro.org database; Tripathy et al., 2015, see Table 1).

After the validation, we have implemented the two biophysical models in reconstructed morphologies from WT and APP/PS1 mice (see Table 2 for their electrophysiological features) and used them in all simulations.

### Excitatory and inhibitory synapses and their activation in model CA1 PCs

AMPA synapses were used as excitatory input for both active CA1 PC spiking models by Jarsky et al. (2005) and Poirazi et al. (2003b). Synapses were implemented as a dual-exponential of time-dependent conductances with rise time constant of  $\tau_1 = 0.2$  ms and decay time constant of  $\tau_2 = 2.5$  ms while having a reversal potential of 0 mV (Exp2Syn NEURON object). The synapses were driven by VecStim point processes in artificial point neurons with generated Poisson spike trains (T2N function `t2n_poissonSpikeGen`). The specific Poisson process frequency varied per protocol and is indicated for each simulation in the figure caption. The synaptic weights had a strength of 0.1nS and synapse density was homogeneous with 0.5 synapses/ $\mu\text{m}$  for the simulations, in which only AMPA was implemented.

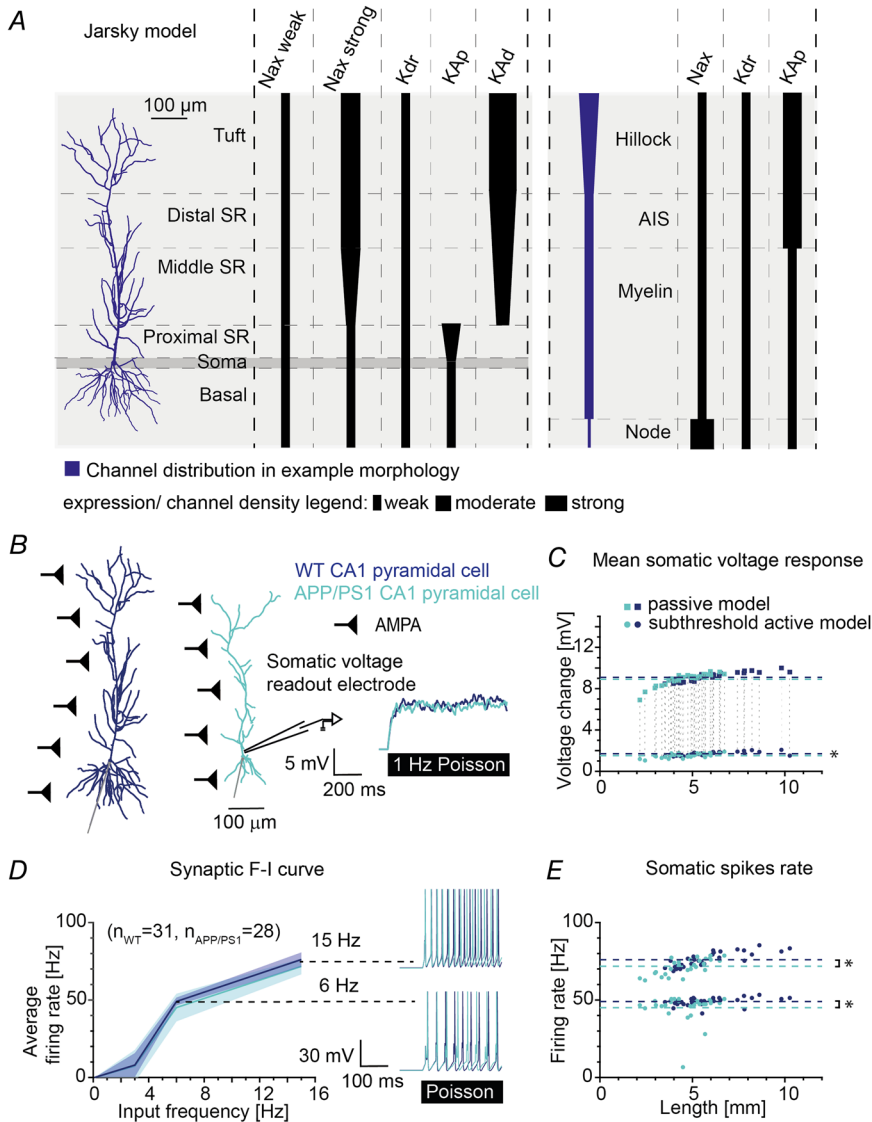


**Figure 3. Responses to distributed synaptic inputs show no hyperexcitability in APP/PS1 morphologies with the biophysical model by Jarsky et al. (2005)**

**A**, schematic summary of the ion channel composition of the CA1 pyramidal cell model with biophysics by Jarsky et al. (2005). Left, an exemplar reconstructed morphology used for the compartmental modelling. Right, distribution of ion channel density. The relative thickness of the lines indicates the channel density. **B**, left: same experimental set-up as in Poirazi model (see Results) but with ion channel model by Jarsky et al. (2005) (WT in dark blue, APP/PS1 in light blue). Right, sample trajectories for the voltage response of the two sample cells for the passive model with whole cell distributed AMPA stimulation of 1 Hz Poisson inputs. **C–E**, passive and active model simulations depicting voltage change response and firing rate versus dendritic length and input frequency respectively with the model by Jarsky et al. (2005). The asterisks indicate significant differences. [Colour figure can be viewed at [wileyonlinelibrary.com](http://wileyonlinelibrary.com)]



**Table 1. Comparison of e-phys features between the original NEURON models (Jarsky et al., 2005; Poirazi et al., 2003a,b) and their T2N versions, and between NeuroMorpho models and NeuroElectro data**

Spiking features	Poirazi:		Poirazi:		Poirazi:		Poirazi:		Jarsky:		Jarsky:		Neuro-Electro data	
	original model (rat)	T2N version	Neuro-Morpho model	original model (rat)	T2N version	original model (rat)	T2N version	Neuro-Morpho model	original model (rat)	T2N version	Neuro-Morpho model	original model (rat)	T2N version	Neuro-Electro data (rat)
Input resistance (MΩ)	65.25	64.16	167.43 ± 48.41	67.72	68.46	67.72	68.46	202.62 ± 73.39	107.00 ± 77.58					
Total capacitance (pF)	115.60	110.88	69.91 ± 13.25	81.84	80.93	81.84	80.93	53.77 ± 13.25	89.80 ± 53.65					
Time constant (ms)	11.02	12.68	12.30 ± 1.54	7.74	7.59	7.74	7.59	9.71 ± 0.57	24.50 ± 21.49					
Resting potential (mV)	-68.40	-68.40	-68.45 ± 0.24	-71.95	-72.25	-71.95	-72.25	-72.63 ± 0.30	-65.23 ± 4.89					
Spike threshold (mV)	-58.60	-58.51	-59.33 ± 0.29	-62.92	-62.30	-62.92	-62.30	-51.36 ± 1.80	-47.60 ± 7.73					
Spike amplitude (mV)	80.00	77.88	79.77 ± 3.82	97.93	97.51	97.93	97.51	87.81 ± 2.02	86.36 ± 12.26					
Spike peak (mV)	21.11	19.33	19.78 ± 4.05	34.93	35.05	34.93	35.05	36.14 ± 1.43	31.74 ± 13.29					
Spike width (ms)	1.77	1.75	1.69 ± 0.09	0.82	0.82	0.82	0.82	0.78 ± 0.05	1.32 ± 0.61					
AHP amplitude (mV)	1.67	1.30	2.43 ± 1.27	5.80	7.28	5.80	7.28	17.71 ± 2.09	6.96 ± 5.22					
Rheobase (pA)	120	130	24 ± 0.01	130	150	130	150	103 ± 0.03	189 ± 287					

AHP, afterhyperpolarisation.

In the main results and in Fig. 4B, additionally to AMPA synapses we implemented NMDA synapses with slower kinetics and non-linear voltage-dependence. The NMDA synapses included a magnesium block removed by sufficient depolarisation. The synapses followed a dual-exponential slower than the AMPA synapses with rise time constant of  $\tau_1 = 0.33$  ms and decay time constant of  $\tau_2 = 50$  ms while having a reversal potential of 0 mV (Exp2nmda2 NEURON object based on the model from Krueppel et al., 2011). We additionally tested prolonged extracellular glutamate transients, which were reported to be caused by amyloid- $\beta$  accumulation, in Fig. 4B. For this, we increased  $\tau_2$  to 100 ms. All NMDA synapses had the same location as the AMPA synapses and were driven by the same presynaptic Poisson processes.

To model inhibitory synapses, we included GABA-A synapses in the spiking model by Poirazi et al. (2003b). GABA-A synapses were implemented by using the Exp2Syn NEURON object with the same kinetics as for the AMPA synapses but with a changed reversal potential of -70 mV. The weights of the GABA-A synapses had a strength of 2 nS corresponding to values found by Bloss et al. (2016).

For more realistic simulations of synaptic distribution, the densities of the AMPA, NMDA and GABA-A synapses were changed depending on the dendritic region, based on the data from Megias et al. (2001); Šišková et al. (2014); Bloss et al. (2016) (Table 3). Experiments (Šišková et al., 2014) have shown that the spine (and therefore likely also AMPA synapse) density in APP/PS1 morphologies is similar to the spine density in WT morphologies in all dendritic regions except for the tuft region where it is reduced to 82.3% of WT synapse density. Therefore, we have used equal densities in all dendritic layers of WT and APP/PS1 model cells except for the tuft layer.

It has been shown that apical synaptic weights in CA1 PCs are not constant but increase for AMPA (and decrease for NMDA) synapses with distance to soma (Katz et al., 2009; Kim et al., 2015; Magee & Cook, 2000). Therefore, to implement a realistic inhomogeneous synaptic weight distribution, the apical AMPA synapses were up-scaled and NMDA down-scaled in a linear distance-dependent manner for the model by Poirazi et al. (2003b). Along the somato-dendritic axis the AMPA synapses followed the relation  $g_{AMPA} = (0.4 + p) \times scale_{AMPA}$  for the conductance values, while  $scale_{AMPA}$  corresponded to 0.1 nS and  $p$  corresponded to the path-length from soma to synapse location  $x$  normalised to the maximum path-length of the cell  $p = path(x)/max[path(cell)]$  resulting in increasing weights with increasing distance to soma with a strength of 0.04–0.14 nS. The NMDA synapses followed the relation  $g_{NMDA} = (1.2 - 0.4 \times p) \times scale_{NMDA}$  with  $scale_{NMDA} = 0.1$  nS resulting in decreasing NMDA weights with increasing distance to soma with a strength of 0.08–0.12 nS. The slope was estimated by

**Table 2.** Major e-phys features of the two biophysical models (Jarsky et al., 2005; Poirazi et al., 2003a,b) implemented in reconstructed WT and APP/PS1 PC morphologies (mice) using T2N

Spiking features	Poirazi: WT model cells	Poirazi: APP/PS1 model cells	Jarsky: WT model cells	Jarsky: APP/PS1 model cells
Input resistance (M $\Omega$ )	117.04 $\pm$ 22.11	133.70 $\pm$ 33.15	212.05 $\pm$ 60.74	262.68 $\pm$ 94.45
Total capacitance (pF)	96.92 $\pm$ 31.55	75.85 $\pm$ 20.42	54.22 $\pm$ 18.88	41.68 $\pm$ 12.37
Time constant (ms)	9.29 $\pm$ 1.10	8.34 $\pm$ 0.90	12.51 $\pm$ 1.30	12.90 $\pm$ 1.92
Resting potential (mV)	-68.39 $\pm$ 0.20	-68.40 $\pm$ 0.34	-71.38 $\pm$ 0.29	-71.38 $\pm$ 0.47
Spike threshold (mV)	-60.07 $\pm$ 0.34	-59.99 $\pm$ 0.16	-53.80 $\pm$ 5.30	-55.57 $\pm$ 5.98
Spike amplitude (mV)	81.04 $\pm$ 3.02	82.25 $\pm$ 3.26	89.56 $\pm$ 5.75	91.37 $\pm$ 6.11
Spike peak (mV)	20.97 $\pm$ 3.05	22.25 $\pm$ 3.30	35.75 $\pm$ 1.66	35.80 $\pm$ 1.17
Spike width (at -30 mV) (ms)	1.46 $\pm$ 0.11	1.43 $\pm$ 0.06	0.79 $\pm$ 0.05	0.79 $\pm$ 0.04
AHP amplitude (mV)	1.40 $\pm$ 0.20	1.31 $\pm$ 0.26	17.05 $\pm$ 5.83	14.91 $\pm$ 6.90
Rheobase (pA)	33 $\pm$ 14	28 $\pm$ 12	119 $\pm$ 38	95 $\pm$ 35

AHP, afterhyperpolarisation.

applying depolarising inputs to the morphology trunks and adjusting the weights depending on distance to soma in order to guarantee the same somatic excitatory postsynaptic potential in agreement with data showing dendritic democracy (Häusser, 2001; Magee & Cook,

2000). In line with experimental data (Bittner et al., 2012), synaptic weights in the tuft stayed constant with the maximum distance value of the aforementioned relations. At the same time, a lognormal ( $\mu = -1.5$ ,  $\sigma = 0.9$ ) term was added to the excitatory conductances (weighted with

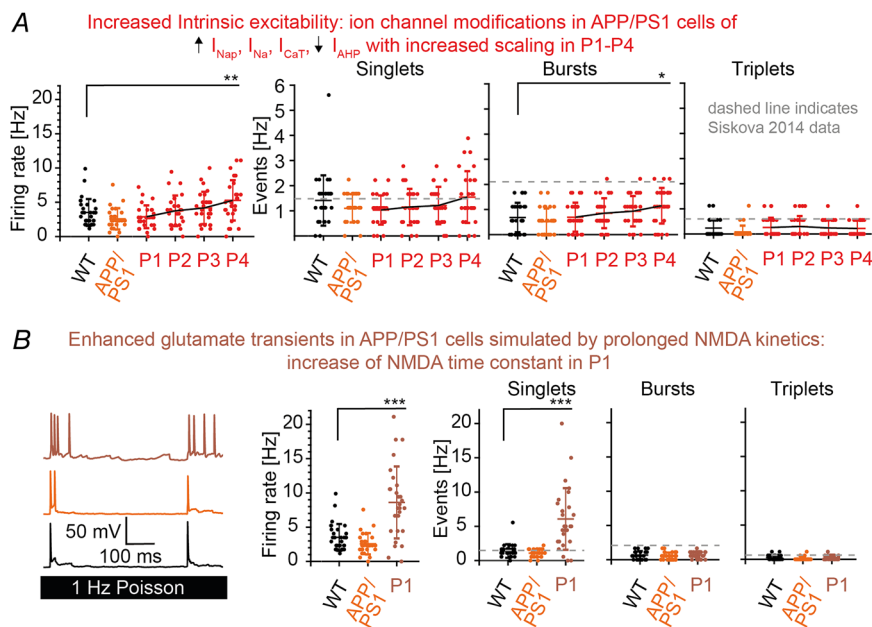


**Figure 4.** Qualitative but not quantitative reproduction of increased burst firing in APP/PS1 cells due to isolated ion channel changes and failed reproduction of increased burst firing due to isolated enhancement of glutamate transients simulated as prolonged NMDA kinetics

**A**, left, overall firing rate in WT (black), APP/PS1 (orange) and APP/PS1 cells with intrinsic ion channel changes (P1–P4, red: increased  $I_{NaP}$ ,  $I_{Na}$ ,  $I_{CaT}$  densities, decreased  $I_{AHP}$  density; see details in Table 4). The asterisks denote a significant increase in firing rate between WT and P4 with  $P = 0.00301$ . Right, number of events for the same cell groups: single APs, bursts (>1 AP) and triplets. The dashed lines indicate data from Šišková et al. (2014). The asterisk indicates a significantly increased burst rate between WT and P4 with  $P = 0.0112$ . **B**, left, Example traces of WT (black), APP/PS1 (orange) and APP/PS1 cells with the enhancement of extrinsic glutamate transients simulated as increased NMDA decay time constant (P1, brown:  $\tau_{P1,NMDA} = 2 \tau_{WT,NMDA}$ ). Middle, overall firing rate of the same groups. The asterisks denote  $P < 0.0001$ . Right, number of events: single APs, bursts and triplets. The asterisks indicate  $P < 0.0001$  for an increased single spike rate between WT and P1 with increased NMDA decay. [Colour figure can be viewed at [wileyonlinelibrary.com](http://wileyonlinelibrary.com)]

scale<sub>AMPA</sub>/2 and scale<sub>NMDA</sub>/2, respectively) to increase their variance and convert the weights into a more realistic distribution with a majority of weak and a minority of strong weights (Arellano et al., 2007; Ballesteros-Yáñez et al., 2006; Benavides-Piccione et al., 2013; Bromer et al., 2018; Katz et al., 2009).

The synaptic inputs were modelled as transient conductance changes (see above) following APs generated from a presynaptic spike generator. In all simulations the CA1 model cells were subject to ongoing background activity generated randomly as Poisson spike trains, with an average spiking frequency that ranged from 0.1 to 10 Hz for AMPA synapses in passive and active models with biophysics by Poirazi et al. (2003b) and 0.5–15 Hz in models with biophysics by Jarsky et al. (2005). The AMPA, NMDA and GABA synapses in active spiking models received an input of 0.5 Hz for both WT and APP/PS1 groups. We increased the excitatory input frequency to AMPA/NMDA inputs to 1 Hz in simulations with strong perisomatic GABAergic inhibition in the high  $\gamma$  range of 50–100 Hz (Craig & McBain, 2015; Strüber et al., 2017). Such stimulation was sufficient to create spontaneous burst firing patterns (inter-spike-interval (ISI)  $\leq$  13.3 ms).

In addition to spontaneous background activity, neuronal firing was driven also by specific input pathways from the connecting network, which was implicitly simulated using spike generators. Therefore, on top of background noise we added correlated theta input of 5 Hz to the excitatory synapses in tuft (perforant pathway), basal (Schaffer collateral basal pathway) and apical (Schaffer collateral apical pathway) dendritic regions of the CA1 cells (Ang et al., 2005; Bannister & Larkman, 1995; Loópez-Madrona et al., 2021; Manns et al., 2007; Megías et al., 2001; Takahashi & Magee, 2009). Therefore, to guarantee a correlation of 0.3 of the input spike trains from each pathway, a modified spike generator was used that kept a random spike train with a probability equal to the target correlation for the next synapse's input spike train (t2n\_poissonSpikeGen2).

### Parameter configurations of AD-related extrinsic and intrinsic changes and their combinations

In total, we explored 11 configurations of parameter changes and their effects on simulated synaptic activation of APP/PS1 CA1 PCs (see Table 4). These configurations

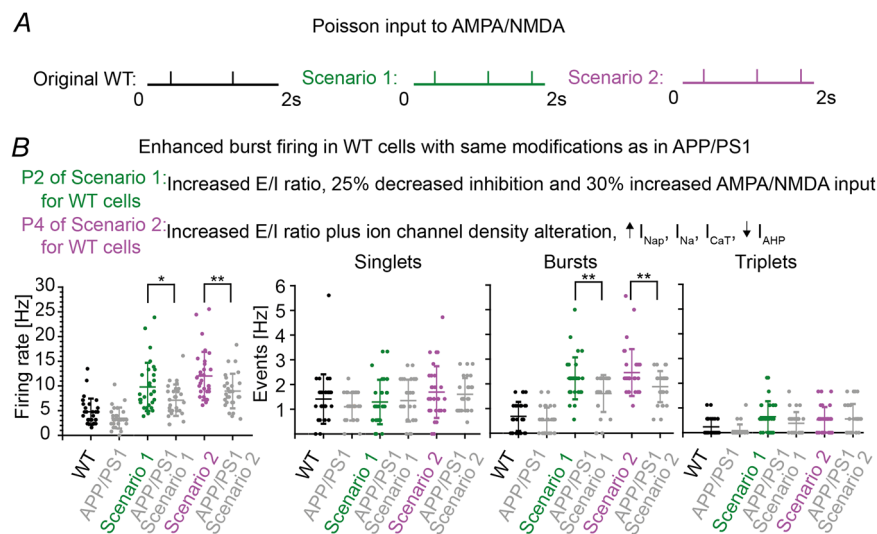


**Figure 5. Control simulations in WT morphologies with altered extrinsic (network) and intrinsic (ion channel) properties as in APP/PS1 morphologies lead to a stronger transition from solitary to burst firing in WT than in APP/PS1 morphologies**

A, example Poisson input pattern with 1 Hz frequency to AMPA/NMDA synapses of original WT cells (black), and input pattern with 1.3 Hz frequency of scenario 1 (green: increased  $E/I$  ratio) and scenario 2 (purple: increased  $E/I$  ratio plus ion channel alterations) for WT cells. B, left, overall firing rate for original WT cells (black), scenario 1 for WT cells (green) and scenario 2 for WT cells (purple). The original APP/PS1 cells and the APP/PS1 cells in scenario 1 and 2 are shown in grey. The modified WT cells of both scenarios show a stronger increase in firing rate than the corresponding modified APP/PS1 cells: extrinsic changes of scenario 1 with  $P = 0.0164$ , extrinsic/intrinsic changes of scenario 2 with  $P = 0.00871$  as indicated by the asterisks. Right, number of events for the same cell groups: single APs, bursts ( $>1$  AP) and triplets. For burst firing, modified WT cells of both scenarios show a stronger increase in burst rate than the corresponding modified APP/PS1 cells: extrinsic changes of scenario 1 with  $P = 0.00469$ , extrinsic/intrinsic changes of scenario 2 with  $P = 0.00939$  as indicated by the asterisks. [Colour figure can be viewed at [wileyonlinelibrary.com](http://wileyonlinelibrary.com)]

included extrinsic and intrinsic changes (altered  $E$  and  $I$  input, enhanced network burst input, scaling of ion channel densities  $I_{AHP}$ ,  $I_{Nap}$ ,  $I_{Na}$  and  $I_{CaT}$ ), as well as their possible combinations (changes in:  $E/I$  ratio, bursts +  $I$ , channels +  $E$ , channels +  $I$ , channels +  $E/I$ , bursts + channels, burst + channels +  $I$ ). For each configuration we implemented a four-step incremental alteration of parameters from P1 to P4. Starting with the parameter set-up for the WT cell group, we increasingly modified the respective parameters in the APP/PS1 cell group to eventually achieve a similar spike rate and pattern as in the Table 5 (data from Šišková et al., 2014). Further variation of the parameters was continued until the firing rate and burst rate diverged again from the data in Šišková et al. (2014).

For the configuration *Excitation*, the Poisson frequency of the excitatory input to the AMPA/NMDA synapses was enhanced from the control 'P0' value of 1 Hz to P1 of 1.1 Hz, up to P4 of 1.8 Hz. For the same configuration, the input correlation ranged from P1 of 0.7 to P4 of 1. Furthermore, for the configuration *Inhibition*, the GABA synapse density was reduced step-wise from P1 of 75% to P4 of 35%. For the configuration *Burst input*, we fed

spike trains of elevated burst activity to 4% of excitatory synapses (Table 3). In line with the range of firing rates and burst patterns from *in vivo* patch-clamp recordings in healthy cells (Table 5; Šišková et al., 2014), WT and control ('P0'). APP/PS1 model cells received four singlets and one doublet per 2 s per synapse (input frequency 3 Hz, input burst frequency 0.5 Hz, ISI 10 ms), whereas the modified APP/PS1 model cells received more and stronger bursts from P1 (input frequency 4 Hz, input burst frequency 1 Hz) to P4 (input frequency 8.5 Hz, input burst frequency 2.5 Hz). The coefficient of variation (CV) for the input frequency per cell in all cases was 0, since all stimulated synapses got the same number of input spikes. The configurations containing combinations of changes included combined alterations of the same parameters. The individual parameters were varied less strongly but within the same range. A complete overview of all parameter configurations is given in Table 4.

### Cost functions

To compare the results of our simulations with the experimental results of Šišková et al. (2014), we used an

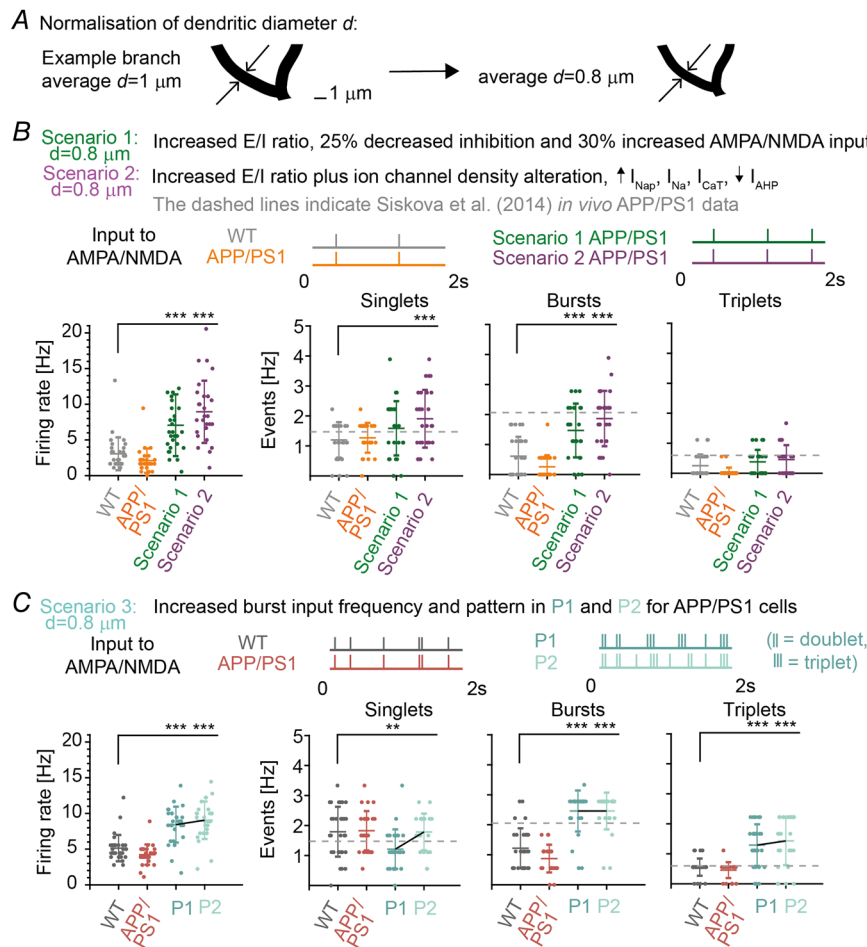


**Figure 6. Control simulations of morphologies with an average dendritic diameter of  $0.8 \mu\text{m}$  modified by extrinsic and intrinsic changes lead to a similar increase in burst firing in APP/PS1 cells as simulations with the average diameter of  $1 \mu\text{m}$**

A, left, example branch of a reconstructed CA1 pyramidal cell with normalised dendritic diameter to ensure an overall average target diameter of the whole dendritic tree of  $d = 1 \mu\text{m}$ . Right, the normalised average dendritic diameter was reduced to  $d = 0.8 \mu\text{m}$  according to Benavides-Piccione et al. (2020). B, top, input pattern to original WT (grey), APP/PS1 (orange) and APP/PS1 for scenario 1 (green: increased  $E/I$  ratio) and scenario 2 (purple: increased  $E/I$  plus channel alterations). Bottom, burst firing for scenario 1 and 2 with normalised dendritic diameter of  $d = 0.8 \mu\text{m}$ . Throughout the figure,  $*P < 0.05$ ,  $**P < 0.01$  and  $***P < 0.001$ . C, top, input burst pattern to original WT (dark-grey), APP/PS1 (dark-orange) and APP/PS1 for scenario 3 (P1–P2, turquoise: increased burst frequency). Bottom, burst firing for scenario 3 with normalised dendritic diameter of  $d = 0.8 \mu\text{m}$ . [Colour figure can be viewed at [wileyonlinelibrary.com](http://wileyonlinelibrary.com)]

error function (Error) that measures the distance between simulation (Sim) and experiment (Exp) via a root mean squared error normalised by the root of the squared standard error of the mean (SEM) (Borst & Haag, 1996):

$$\text{Error}_{\text{Sim}} = \sum_{\text{Firing mode}} (\mu_{\text{Firing, Sim}} - \mu_{\text{Firing, Exp}})^2 \quad (1)$$

$$\text{Error}_{\text{Exp}} = \sum_{\text{Firing mode}} (\text{SEM}_{\text{Firing, Exp}})^2 \quad (2)$$

$$\text{Error} = (\text{Error}_{\text{Sim}}/\text{Error}_{\text{Exp}})^{1/2} \quad (3)$$

The sum over firing modes included singlets (1 AP), bursts (>1 AP) and triplets (3 AP) with the experimental values taken from Table 5 (Šišková et al., 2014). Additionally, the error included the change in the firing mode from singlet to bursts (see Results):

$$\mu_{\text{Singlets}} > \mu_{\text{Bursts}} \rightarrow \text{mode} = 1 \quad (4)$$

$$\mu_{\text{Singlets}} < \mu_{\text{Bursts}} \rightarrow \text{mode} = -1 \quad (5)$$

This was considered in the evaluation and interpretation of simulations since data show a distinct mode transition from singlets to bursts (Šišková et al., 2014). Therefore, models with a clear qualitative transition to bursts represent a better match to the data than models with a small quantitative error in firing rates, but firing mainly singlets. These two costs were analysed and compared in the main results.

### Parameters of the three scenarios

The three scenarios showing increased firing rates and the change in the firing mode from singlets to bursts contained the following parameters.

In scenario 1 (*E/I imbalance*), the best match to the data was achieved by the parameter variation P3 (see Results) comprising increased Poisson input frequency (increased from 1 to 1.3 Hz) and stronger spike train correlations (increased from 0.4 to 0.9) combined with diminished inhibitory inputs (40% decrease of dendritic and somatic inhibition). The CV of the input per cell was 0.41 (WT), 0.41 (APP/PS1) and 0.16 (P3 of APP/PS1). This was due to higher mean input frequency and smaller variation. A further increase of input frequency or impairment of inhibition in P4 of scenario 1 worsened the reproduction with data.

In scenario 2 (*Channels plus E/I*) the best match to the data was achieved by the parameter variation P4, which was comparable to scenario 1 but comprised a milder reduction of inhibition (25% decrease) and additional scaling of ion channel densities (1.3 for  $I_{\text{Na}}$ , 0.8 for  $I_{\text{AHP}}$  and 2.5 for  $I_{\text{Nap}}$  and  $I_{\text{CaT}}$ ). In this scenario, the CV per

cell input was 0.41 (WT), 0.41 (APP/PS1) and 0.17 (P4 of APP/PS1).

In scenario 3 (*Burst input*) we modelled a pre-synaptic control network with burst input to 4% of the AMPA/NMDA synapses using four singlets and one doublet per 2 s (WT, see Results). In contrast, we modelled enhanced network burst input using an increasing number of bursts in the parameter variations P1–P4. The closest match with the data was seen for P3: synaptic input of one singlet, two doublets and three triplets per 2 s (see input pattern and time profile in Results). Importantly, a different input spike train of one less burst or one more singlet (P2 and P4 in Results) showed a higher error and no change in the firing mode from singlets to bursts.

All these extrinsic and intrinsic parameter changes together with an overview of all possible eleven configurations are shown in Table 4.

### Intrinsic ion channel modifications

AD-related changes of ion channels were modelled by modifying their respective conductances according to experimental reports and our *in silico* parameter scans (see Results). To reduce ion channel expression or increase its density, the maximum channel conductance was scaled by a corresponding factor. Specifically, the voltage-dependent sodium channel  $I_{\text{Na}}$  in the axon (Ghatak et al., 2019; Liu et al., 2015; Wang et al., 2016) was scaled up in the range [1, 2] and the persistent sodium channel  $I_{\text{Nap}}$  in the soma (Beck & Yaari, 2008; Williams & Stuart, 1999; Yue et al., 2005) was scaled up in the range [1, 3]. At the same time the medium after-hyperpolarisation calcium-activated potassium channel  $I_{\text{AHP}}$  in the soma and apical dendrites was scaled down in the range [0.3, 1] (Beck & Yaari, 2008; Niday & Bean, 2021; Wang, Kang et al., 2015; Wang, Zhang et al., 2015; Zhang et al., 2014), while the T-type calcium channel  $I_{\text{CaT}}$  in dendrites (Beck & Yaari, 2008; Cain & Snutch, 2013; Garg et al., 2021; Medlock et al., 2018; Yaari et al., 2007) was scaled up in the range [1, 3]. Subsequently, the four-dimensional parameter space of the four channels was scanned and the error function compared to data of Šišková et al. (2014) calculated using Eqn (3). The dependence of each channel scaling on the other channels was then displayed in the main results. A minimum error for the chosen parameter range was found at a scaling of, for example, 1.3 for  $I_{\text{Na}}$ , 0.5 for  $I_{\text{AHP}}$  and 2.5 for  $I_{\text{Nap}}$  and  $I_{\text{CaT}}$ . As a targeted sensitivity check we looked closer in the vicinity of the ion channel scaling that increased bursting and lowered the error [1.1, 1.2, 1.3, 1.4, 1.5] for  $I_{\text{Na}}$  and [0.35, 0.45, 0.5, 0.55, 0.65] for  $I_{\text{AHP}}$ . We did not look beyond values of 3 for  $I_{\text{Nap}}$  and  $I_{\text{CaT}}$  as they seem biologically unrealistic and not supported by the literature, though it is possible that such scaling could

**Table 3. Model synapse densities based on data from Megias et al. (2001), Bloss et al. (2016) and Šišková et al. (2014)**

Dendritic region	AMPA, NMDA synapse/ $\mu\text{m}$	GABA synapse/ $\mu\text{m}$
Proximal basal	0.1	0.3
Middle basal	0.3	0.2
Distal basal	2.0	0.06
Proximal apical trunk	0.3	0.3
Distal apical trunk	3.5	0.06
Proximal apical oblique	2.2	0.05
Distal apical oblique	2.7	0.05
Proximal tuft	1.2	0.2
Distal tuft	0.8	0.2

induce hyperexcitability as well. We were interested in the possibility of channel changes influencing and enhancing burst firing, which we observed in the chosen range (see Results and Fig. 4A, P1–P4). For the configuration *Channels* the firing rate and burst rate was enhanced with increased scaling of ion channels (see Results and Fig. 4A P4: the asterisks denote  $P = 0.00301$  and  $P = 0.0112$  for firing rate and burst rate, respectively), though, importantly, no mode change towards bursts was noticed even when scaling the conductances to extreme values. For the simulations containing ion channel changes, the variation of parameters ranged from P1 (scaling  $I_{\text{Na}} = 1.1$ ,  $I_{\text{AHP}} = 0.8$ ,  $I_{\text{CaT}} = I_{\text{Nap}} = 2.5$ ) to P4 (scaling  $I_{\text{Na}} = 3$ ,  $I_{\text{AHP}} = 0.1$ ,  $I_{\text{CaT}} = I_{\text{Nap}} = 3$ ). A complete list of all configurations of channel parameters is given in Table 4.

It was not within the scope of this study to find a scaling of ion channel conductances that would maximise the burst activity. APP/PS1 model cells reacted with a large variance in firing rates to ion channel modifications indicating that different scaling might increase burst firing for different cells (see Discussion). However, for a valid comparison with other configurations it was necessary to modify all cells in the same manner. Furthermore, we tested also alterations of other ion channels that are mentioned in the literature in relation to AD including potassium and hyperpolarisation-activated, cyclic nucleotide-gated HCN channels, which have been proposed to be involved in hyperexcitability (Beck & Yaari, 2008; Musial et al., 2018; Vitale et al., 2021). However, our simulations did not show an effect on excitability (especially regarding burst firing) of APP/PS1 CA1 PC morphologies. A recent study confirmed that a change in the  $I_{\text{h}}$  channel was not accompanied by a change in intrinsic excitability in experiments with APP/PS1 model cells (Ohline et al., 2022). Modifications in the conductance of the L-type calcium channels also did not enhance burst firing (Anekonda et al.,

2011; Berridge, 2014). It is important to note, that the mentioned channels could play a role in other neuronal properties that have not been relevant for this study and therefore were not tested. For example, HCN channels seem to be important for efficient dendritic integration, which can be enhanced in atrophied dendrites (Dhupia et al., 2015). Likewise, changes in A-type potassium channels might influence for instance the input resistance, impedance and firing frequency (Rathour et al., 2016). Our simulation protocol did not show increased somatic firing, though a previous study showed increased dendritic excitability in neurons with potassium channel alterations observed in a murine model of AD (Hall et al., 2015).

When we performed control simulations by applying the same ion channel and network modifications to WT morphologies (Fig. 1A), we found an even higher increase in burst firing than in APP/PS1 morphologies (Fig. 5B: extrinsic changes in scenario 1 for WT  $2.22 \pm 0.85$  Hz and APP/PS1  $1.61 \pm 0.75$  Hz,  $P = 0.00469$ ; and extrinsic/intrinsic changes in scenario 2 for WT  $2.46 \pm 0.95$  Hz and APP/PS1  $1.88 \pm 0.63$  Hz,  $P = 0.00939$ ). Since WT morphologies have larger sizes than APP/PS1 morphologies (due to the lack of dendritic degeneration), this is in agreement with previous studies showing elevated burst firing for larger cells (van Elburg & van Ooyen, 2010). Accordingly, a smaller dendritic size would reduce synaptically driven burst firing suggesting that dendritic degeneration may serve as a compensatory mechanism.

Pyramidal cells typically have an average dendritic diameter of  $0.8 \mu\text{m}$  (Benavides-Piccione et al., 2020). However, the reconstructed cells in this study had a higher diameter of  $1.6 \mu\text{m}$  on average (Fig. 1A; see above 'Dendrite morphologies'). Since the diameter variation could influence the firing behaviour, we performed control simulations (Fig. 6) with the diameter of  $0.8 \mu\text{m}$  but observed similar behaviour as in the main results.

### Statistical analysis

We used an unpaired Student's  $t$  test for the statistical comparison of morphological parameters (path length, number of branch points, surface area, dendritic diameter), voltage change and firing rate in WT and APP/PS1 groups. When we assessed the statistical significance of differences in firing rate and event rate (singlets, bursts, triplets) between the WT, APP/PS1 groups and the APP/PS1 group with modified extrinsic and intrinsic properties we used one-way ANOVA. All error bars are shown with mean and standard deviation. A value of  $P < 0.05$  was considered significant and depicted with an asterisk.

**Table 4. All explored extrinsic and intrinsic parameter configurations**

Configuration	Feature	Control	Variation				
			P1	P2	P3	P4	
Excitation	Input frequency	1 Hz	1.1 Hz	1.3 Hz	1.6 Hz	1.8 Hz	
	Input correlation	0.4	0.7	0.8	0.9	1	
Inhibition	% GABA activation	100	75	60	45	35	
	Scenario 1: E/I imbalance	Input frequency	1 Hz	1.1 Hz	1.3 Hz	1.3 Hz	1.3 Hz
		Input correlation	0.4	0.7	0.8	0.9	1
Channels	% GABA activation	100	50	75	60	50	
	Scale $I_{Na}$	1	1.1	1.3	1.5	3	
	Scale $I_{Nap}$	1	2.5	2.5	2.5	3	
	Scale $I_{CaT}$	1	2.5	2.5	2.5	3	
Channels plus excitation	Scale $I_{AHP}$	1	0.8	0.5	0.3	0.1	
	Input frequency	1 Hz	1.1 Hz	1.2 Hz	1.3 Hz	1.3 Hz	
	Input correlation	0.4	0.7	0.8	0.9	0.9	
	Scale $I_{Na}$	1	1.3	1.3	1.3	1.5	
	Scale $I_{Nap}$	1	2.5	2.5	2.5	2.5	
Channels plus inhibition	Scale $I_{CaT}$	1	2.5	2.5	2.5	2.5	
	Scale $I_{AHP}$	1	0.5	0.5	0.5	0.3	
	% GABA activation	100	70	60	50	50	
	Scale $I_{Na}$	1	1.3	1.3	1.3	1.5	
	Scale $I_{Nap}$	1	2.5	2.5	2.5	2.5	
Scenario 2: channels plus E/I imbalance	Scale $I_{CaT}$	1	2.5	2.5	2.5	2.5	
	Scale $I_{AHP}$	1	0.5	0.5	0.5	0.3	
	Input frequency	1 Hz	1.1 Hz	1.1 Hz	1.1 Hz	1.3 Hz	
	Input correlation	0.4	0.7	0.7	0.8	0.9	
	% GABA activation	100	60	70	60	75	
	Scale $I_{Na}$	1	1.3	1.5	1.5	1.3	
Scenario 3: burst input	Scale $I_{Nap}$	1	2.5	2.5	2.5	2.5	
	Scale $I_{CaT}$	1	2.5	2.5	2.5	2.5	
	Scale $I_{AHP}$	1	0.5	0.3	0.3	0.8	
	Input frequency	3 Hz	4 Hz	6 Hz	7 Hz	8.5 Hz	
	Input burst frequency	0.5 Hz	1 Hz	2 Hz	2.5 Hz	2.5 Hz	
Burst input plus inhibition	Input frequency	3 Hz	6 Hz	6 Hz	7 Hz	7 Hz	
	Input burst frequency	0.5 Hz	2 Hz	2 Hz	2.5 Hz	2.5 Hz	
	% GABA activation	100	80	50	80	50	
Burst input plus channels	Input frequency	3 Hz	4 Hz	6 Hz	7 Hz	7.5 Hz	
	Input burst frequency	0.5 Hz	1 Hz	2 Hz	2.5 Hz	2.5 Hz	
	Scale $I_{Na}$	1	1.3	1.3	1.3	1.3	
	Scale $I_{Nap}$	1	2.5	2.5	2.5	2.5	
	Scale $I_{CaT}$	1	2.5	2.5	2.5	2.5	
Burst input, inhibition and channels	Scale $I_{AHP}$	1	0.5	0.5	0.5	0.5	
	Input frequency	3 Hz	4 Hz	6 Hz	6 Hz	7 Hz	
	Input burst frequency	0.5 Hz	1 Hz	2 Hz	2 Hz	2.5 Hz	
	% GABA activation	100	80	80	50	50	
	Scale $I_{Na}$	1	1.3	1.3	1.3	1.3	
	Scale $I_{Nap}$	1	2.5	2.5	2.5	2.5	
	Scale $I_{CaT}$	1	2.5	2.5	2.5	2.5	
	Scale $I_{AHP}$	1	0.5	0.5	0.5	0.5	

**Table 5. Single spikes, bursts and triplets in *in vivo* whole-cell patch-clamp recordings from CA1 PCs in WT and APP/PS1 mice (from figure 1B in Šišková et al., 2014)**

	Singlets (1 AP)	Bursts (>1 AP)	Triplets (3 AP)
Mean $\mu_{WT}$ (Hz)	1.54	0.84	0.16
SEM <sub>WT</sub>	0.43	0.22	0.04
Mean $\mu_{APP/PS1}$ (Hz)	1.47 n.s.	2.06*	0.60*
SEM <sub>APP/PS1</sub>	0.51	0.31	0.10

Note predominantly burst firing vs. solitary firing in APP/PS1 vs. WT mice, respectively. \*Significant; n.s., not significant.

## Results

Dendritic degeneration is a prominent feature observed in AD (Baloyannis, 2009). However, its functional consequences have not yet been fully understood. Investigating whether dendritic degeneration alone is sufficient to account for the pathologically increased neuronal excitability observed in AD (Vossel et al., 2017) is only possible with computational models that allow for isolated manipulations of morphological parameters. Therefore, we implemented a data-driven, biophysically and anatomically realistic compartmental model of

wild-type (WT) and APP/PS1 CA1 pyramidal neurons. We examined the impact of dendritic morphology on the cell's output behaviour by using a previously published morphological data set of 31 WT and 28 APP/PS1 CA1 pyramidal neurons from a mouse model of AD (Šišková et al., 2014). These morphological data were used to create neuronal models in the simulation environment T2N (Beining et al., 2017). A representative morphology from each cell group is shown in Fig. 7A.

To simulate *in vivo*-like conditions, where a single cell integrates the synaptic inputs from different locations across the whole dendritic tree, we uniformly distributed

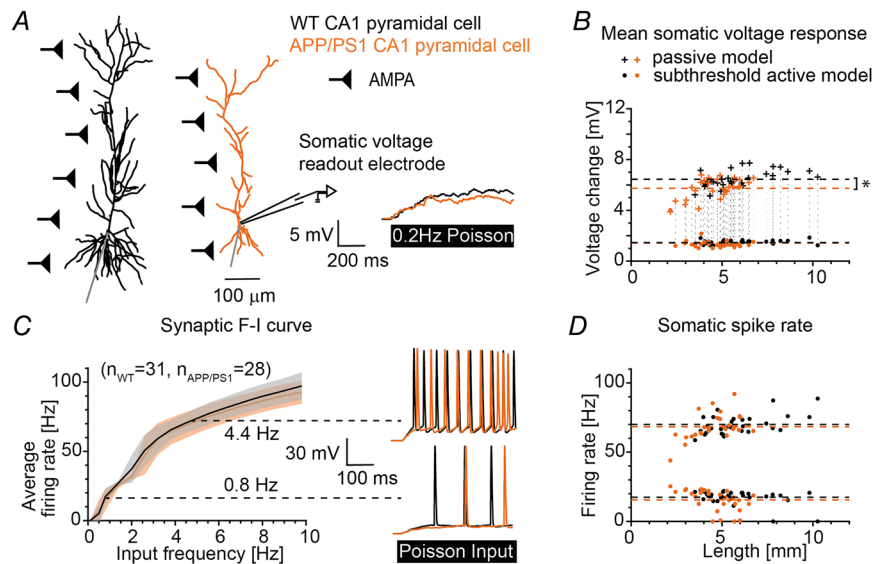


**Figure 7. Responses to distributed synaptic AMPA inputs show that dendritic degeneration by itself causes no hyperexcitability in APP/PS1 model cells if synaptic density remains preserved**

A, sample 3D-reconstructed morphologies of wild-type (WT, black) and APP/PS1 (orange) CA1 pyramidal cells. Distributed AMPA synapses (black triangles) receiving Poisson input patterns. The inset on the right shows sample trajectories for the voltage response of the two sample cells for the passive model with synaptic stimulation at 0.2 Hz. B, voltage responses to distributed AMPA inputs at 0.2 Hz versus dendritic length for the passive (crosses) and the subthreshold active model by Poirazi et al. (2003b, circles) for all available cell morphologies (WT:  $n = 31$ , APP/PS1:  $n = 28$ ). The dashed lines show the mean activity of the WT (black) and APP/PS1 (orange) CA1 cell groups (the asterisk depicts  $P = 0.000467$ ). C, synaptic input–output (IO) curve for the average somatic firing rate of all WT and APP/PS1 cells in active compartmental models with suprathreshold frequencies of AMPA synapse activation. The input frequency ranged from 0.1 to 10 Hz. The right insets show action potential (AP) firing traces of the two sample cells for an input frequency of 0.8 and 4.4 Hz, respectively. D, firing rate versus dendritic length corresponding to the data points with input frequency of 0.8 and 4.4 Hz in C. The dashed lines show the mean firing rate. [Colour figure can be viewed at [wileyonlinelibrary.com](http://wileyonlinelibrary.com)]



excitatory (AMPA) synapses at a fixed density along the cell's dendritic arbour and induced Poisson-like synaptic background noise, while measuring the cell's response at the soma (Fig. 7A). Importantly, in agreement with the experimental spine density data obtained from the reconstructed morphologies (Šišková et al., 2014), we used the same density of synapses for WT and APP/PS1 morphologies. Implementing an identical density of synapses in both cell groups results, on average, in a smaller absolute number of synapses for the shorter (degenerated) APP/PS1 dendrites. In this simple implicit way we implemented the synapse loss in APP/PS1 mice (see Methods for more details on simulations of synapse density and strength).

### Dendritic degeneration alone does not account for synaptically driven hyperexcitability in APP/PS1 CA1 PC models

Firstly, we investigated the cell's behaviour in the context of electrically passive dendrites. We found that the dendritic degeneration observed in the APP/PS1 morphology group (statistical comparison of morphological measures in Methods) did not lead to an increase in the somatic voltage responses (Fig. 7B, crosses), even though the reduction in cell size increases the cell's input resistance. In fact, the APP/PS1 cell group showed on average a reduced voltage change when compared to the WT group (mean voltage passive model: WT  $6.45 \pm 0.67$  mV, APP/PS1  $5.74 \pm 0.80$  mV, the asterisk depicts  $P = 0.000467$ ). Of note, to visualise the variability of individual model cells, the plots in this and following panels and figures show not only the comparison between WT and APP/PS1 average firing rate (dashed lines) but also the relationship between the firing rate and dendritic length for all morphologies within the WT and the APP/PS1 group.

Secondly, in order to explore neuronal excitability in more realistic active dendrites, we extended the passive model by the insertion of active ion channels from a well-established biophysical CA1 PC model (Poirazi et al., 2003b; ion channel details in Methods). To achieve this, we used a previously established scaling method for transferring distance-dependent ion channel densities to multiple CA1 PC morphologies (Cuntz et al., 2021). The insertion of the ion channels led to a pronounced change in the subthreshold behaviour of neurons in response to synaptic activation, reducing and equalising the voltage responses across both morphology groups (Fig. 7B, circles, mean voltage subthreshold active model: WT  $1.47 \pm 0.17$  mV, APP/PS1  $1.41 \pm 0.51$  mV). Similarly, the spiking behaviour was comparable across both cell groups, displaying overlapping  $F-I$  curves (Fig. 7C) and firing rates that were independent from the

cell's dendritic length and complexity (Fig. 7D, 0.8 Hz input: WT  $17.35 \pm 5.29$  Hz, APP/PS1  $15.40 \pm 7.72$  Hz; 4.4 Hz input: WT  $69.91 \pm 7.23$  Hz, APP/PS1  $68.29 \pm 9.41$  Hz). This remained true for other morphological parameters such as branch points and surface area (Methods).

Together, these results show that the dendritic degeneration observed in the APP/PS1 group does not lead to a facilitation of the synaptic integration for either the passive or active neuron model, when compared to their WT counterparts. Similar results were obtained using a simpler CA1 PC biophysical model (Jarsky et al., 2005, in Methods). Therefore, we can conclude that morphological changes alone cannot account for the cellular hyperexcitability observed in the APP/PS1 mouse model.

### Dendritic degeneration can affect CA1 PC excitability by selective gating of layer-specific inputs

Degeneration can disproportionately affect some dendritic subregions. For example, basal dendrites are generally lost before the more peripheral portions of the apical tree in CA1 PCs (Šišková et al., 2014; Scheibel, 1979). Therefore, we explored whether subregion-specific dendritic degeneration leads to a change in CA1 PC behaviour in response to layer-specific input pathways. For this purpose, we implemented a more realistic distribution of synaptic inputs based on anatomical synaptic data. We incorporated layer-specific synapse densities as well as distance-dependent and lognormal synaptic weight distributions (based on Bloss et al., 2016; Katz et al., 2009; Kim et al., 2015; Magee & Cook, 2000; Megías et al., 2001; Šišková et al., 2014), which included AMPA, NMDA and GABA synapses (Fig. 8A, right insets). We divided the inputs into the three major layer-specific input pathways to the CA1 cell (Fig. 8C, schematic): the perforant path and the apical and basal Schaffer collaterals. Synaptic background activity (Poisson-like), targeting all dendritic regions, did not lead to an increased excitability in the APP/PS1 cell group. Moreover, the spiking behaviour still remained independent from the cell's dendritic length (Fig. 8B, WT  $25.24 \pm 6.74$  Hz, APP/PS1  $23.69 \pm 3.87$  Hz; see comparison with Fig. 7D).

In order to simulate the input coming from each different pathway, we introduced correlated synaptic activity, separately targeting layer-specific subregions within the dendritic tree. In this way, we could test whether a more 'clustered' synaptic activation, coming from particular input pathways, leads to a difference in the response behaviour between the two morphology groups. We simulated a rhythmic activation of the synapses in each of the three input areas (entorhinal cortex input, CA3

input to oblique and basal dendrites) at a theta frequency (5 Hz), which resembles a prominent behavioural input pattern received by the hippocampus (Ang et al., 2005; Bannister & Larkman, 1995; López-Madrona et al., 2021; Manns et al., 2007; Megias et al., 2001; Takahashi & Magee, 2009).

Again, we first looked at the passive cell model in response to the different input pathways (Fig. 8C). We found similar voltage changes in passive WT and APP/PS1 cells evoked by the perforant pathway stimulation (Fig. 8C, left panel: WT  $20.12 \pm 4.05$  mV, APP/PS1  $18.68 \pm 4.72$  mV). However, when stimulating the Schaffer collateral inputs on the apical dendrites, we found slightly larger voltage changes in the APP/PS1 cell group (Fig. 8C, middle panel: WT  $39.48 \pm 7.63$  mV, APP/PS1  $43.26 \pm 6.48$  mV,  $P = 0.0456$ ). Interestingly, this behaviour was reversed when we looked at the voltage change caused by the CA3 input to the basal dendrites (Fig. 8C, right panel: WT  $28.86 \pm 6.31$  mV, APP/PS1  $25.53 \pm 7.10$  mV,  $P = 0.0618$ ). The insertion of active conductances in the cell model (Poirazi et al., 2003b) led to comparable results to the ones shown above for the passive model (compare Fig. 8C and D). The perforant pathway input resulted in

similar firing rates across the WT and APP/PS1 cell groups (Fig. 8D, left panel: WT  $54.07 \pm 9.38$  Hz, APP/PS1  $53.62 \pm 12.47$  Hz). For the apical Schaffer collateral pathway, the APP/PS1 cells displayed marginally larger firing rates when compared to the WT cells (Fig. 8D, middle panel: WT  $84.38 \pm 14.44$  Hz, APP/PS1  $90.31 \pm 13.27$  Hz,  $P = 0.107$ ). In contrast, the CA3 input to the basal dendrites led to a strong correlation between the cell's firing rate and dendritic length, displaying a significant decrease in the average firing rate in APP/PS1 neurons when compared to WT controls (Fig. 8D, right panel: WT  $82.44 \pm 27.70$  Hz, APP/PS1  $67.11 \pm 18.79$  Hz, asterisk depicts  $P = 0.0169$ ).

We hypothesised that these pathway-dependent differences in somatic excitability could be due to the variability found in basal/apical dendritic length ratios across the data set (Fig. 9A, mean ratio WT  $0.55 \pm 0.26$ , APP/PS1  $0.39 \pm 0.22$ , asterisk depicts  $P = 0.0126$ ). A cell with a smaller basal/apical ratio receives relatively less basal input per total dendritic length, and experiences a larger inactivated apical region that acts as a voltage sink, which could then lead to the differences in the firing output.

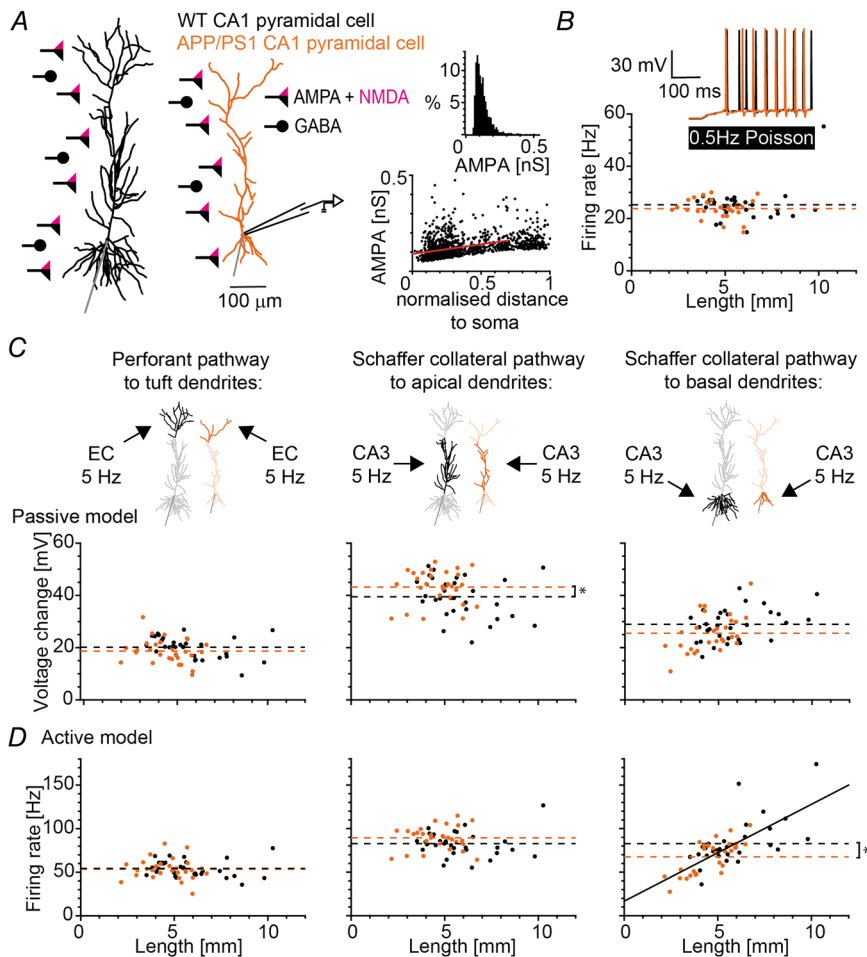


**Figure 8. Responses to activated AMPA, NMDA and GABA synapses of main layer-specific input pathways show that dendritic degeneration by itself can cause changes in excitability in APP/PS1 model cells through selective gating of the inputs**

A, sample morphologies of CA1 pyramidal cells (WT in black, APP/PS1 in orange) with a schematic representation of distributed AMPA (black triangle), NMDA (magenta triangle) and GABA (black circle) synapses (see Methods and Table 3). Right, biologically realistic distribution of AMPA weights with respect to the relative distance to soma (lognormal distribution of synaptic weights with a distance-dependent increase). B, firing rate versus dendritic length of WT and APP/PS1 cells for background noisy input stimulation at 0.5 Hz in a realistic, active CA1 model by Poirazi et al. (2003b). The inset (top right) shows sample voltage responses of the two cells in A. C, voltage change versus dendritic length of WT and APP/PS1 cells for three pathway stimulations of 5 Hz are shown for the passive model of Poirazi et al. (2003b). The dashed lines show the mean voltage responses (the asterisk depicts  $P = 0.0456$ ). D, firing rates versus dendritic length of WT and APP/PS1 cells for the same three pathway stimulations as in C but for the active model by Poirazi et al. (2003b). The dashed lines show the mean firing rate (the asterisk depicts  $P = 0.0169$ ). [Colour figure can be viewed at [wileyonlinelibrary.com](http://wileyonlinelibrary.com)]

To test this hypothesis, we used morphological modelling to scale the WT and APP/PS1 cell morphologies to a fixed 30/70 basal/apical ratio while keeping the total dendritic length the same as in the original morphologies (Fig. 9A, right panel, purple). We found that, after this structural scaling, the strong correlation between the cell's output and dendritic length was lost, leading to an almost identical average voltage change and firing rate for both morphology groups (Fig. 9B, left: perforant pathway, WT  $18.99 \pm 4.02$  mV, APP/PS1  $16.93 \pm 3.91$  mV; middle: apical Schaffer collateral, WT  $41.15 \pm 8.88$  mV, APP/PS1  $41.09 \pm 7.73$  mV; right: basal Schaffer collateral, WT  $28.88 \pm 7.25$  mV, APP/PS1  $28.92 \pm 7.10$  mV; and Fig. 9C, left: perforant pathway, WT  $52.18 \pm 9.34$  Hz, APP/PS1  $52.40 \pm 11.79$  Hz; middle: apical Schaffer collateral, WT  $87.28 \pm 16.62$  Hz, APP/PS1  $87.33 \pm 12.12$  Hz; right: basal Schaffer collateral, WT  $78.02 \pm 23.16$  Hz, APP/PS1  $80.10 \pm 20.41$  Hz).

Taken together, the results in Figs 8 and 9 indicate that the stronger degeneration of basal dendrites compared to apical dendrites observed in APP/PS1 cells may lead to increased firing as a response to the activation of CA3

Schaffer collateral inputs on the oblique dendrites, while leading to decreased firing as a response to the activation of CA3 inputs on the basal dendrites.

### Concomitant network and intrinsic cell changes lead to enhanced excitability in APP/PS1 cells

So far, our model has shown that, although dendritic degeneration can modulate CA1 PC excitability by selectively gating layer-specific inputs, it cannot fully account for the hyperexcitability observed in APP/PS1 mice. Apart from the morphological changes, which we studied until now, changes in the network input as well as in the intrinsic properties of APP/PS1 CA1 PCs could be responsible for their enhanced firing and bursting. Therefore, our next goal was to use *in silico* simulations to clarify the relative contribution of changes in the network input and ion channels and to predict which changes may be most relevant for AD. Our computational analysis focused on disentangling the mechanisms for hyperexcitability that have been observed in AD mouse models.

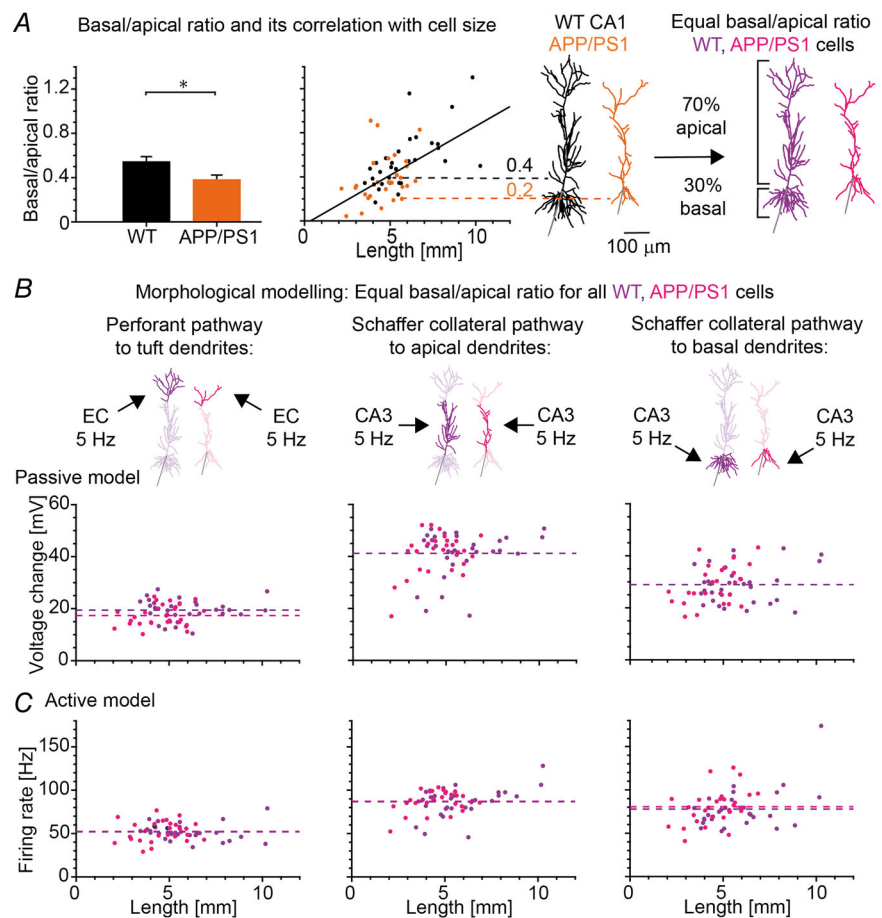


**Figure 9. Morphological modelling with artificially equalized basal/apical dendrite ratios reveals similar responses of WT and APP/PS1 model cells to the activation of main input pathways**  
 A, left, comparison of basal/apical ratio between WT and APP/PS1 cells (asterisk depicts  $P = 0.0126$ ). Middle, basal/apical ratio versus cell length with the continuous black line indicating the linear regression. Right, CA1 morphologies remodelled to equal basal/apical ratio of 30%/70% for all cells (dark purple: WT, light purple: APP/PS1). B and C, similar to Fig. 8C and D but with scaled morphologies of equal basal/apical ratio. [Colour figure can be viewed at [wileyonlinelibrary.com](http://wileyonlinelibrary.com)]

Importantly, in AD, hyperexcitability has been reported not only as a general increase in firing rates, but also as a transition in the firing mode of pyramidal neurons from solitary spikes to bursting (Berridge, 2014; Chen, 2005; Ghatak et al., 2019; Kellner et al., 2014; Minkeviciene et al., 2009; Müller et al., 2021). This shift of the firing mode towards spike bursts has been previously detected in CA1 PCs in the APP/PS1 mouse model of AD (Šišková et al., 2014). However, the mechanism for this is unclear. Therefore, based on the available literature, we investigated the effects of four different configurations of AD-related extrinsic and intrinsic changes in our model: changes in the intensity of excitatory and inhibitory input, alterations in network bursting and modifications in ion channels, and all their possible combinations:

- (1) *Excitation*: increased frequency and correlation of Poisson input to AMPA/NMDA synapses.
- (2) *Burst input*: increased presynaptic burst frequency and pattern.
- (3) *Inhibition*: decreased GABAergic synaptic input.
- (4) *Channels*: scaling of the channel densities  $I_{AHP}$ ,  $I_{Nap}$ ,  $I_{Na}$  and  $I_{CaT}$ .

In addition, possible combinations of these properties comprise further configurations of parameter changes:

- (1) *E/I imbalance* (enhanced  $E$ , reduced  $I$ ).
- (2) *Burst input plus inhibition*.
- (3) *Channels plus excitation*.
- (4) *Channels plus inhibition*.
- (5) *Channels plus E/I*.
- (6) *Burst input plus channels*.
- (7) *Burst input plus inhibition and channels*.

Our goal was to identify those scenarios that could lead to the shift of firing mode observed in Šišková et al. (2014). The contribution of each configuration as well as the change to the burst firing mode were quantified using an error function (root-mean-squared error: Eqs (1)–(3) that compared our *in silico* results with existing data (Šišková et al., 2014; compare Table 5 and Fig. 10). In summary, from our configurations (Fig. 10D), we identified three scenarios where we observed increased burst firing without changes in solitary spike firing (Fig. 11A–C), as observed experimentally in APP/PS1 PCs in mice.

**Scenario 1: increased extrinsic  $E/I$  ratio with increased excitatory and decreased inhibitory input.** Both enhanced excitatory glutamatergic (Busche & Konnerth, 2016; Zott et al., 2019) and impaired inhibitory GABAergic transmission have been shown to contribute to neuronal network dysfunction in AD (Ambrad Giovannetti & Fuhrmann, 2019; Busche et al., 2008; Gervais et al., 2022; Hijazi et al., 2020; Melgosa-Ecenarro

et al., 2022; Palop & Mucke, 2016; Ruiter et al., 2020; Schmid et al., 2016; Xu et al., 2020; but see also Hollnagel et al., 2019). Based on our parameter scan (Fig. 10D), we found that an increased  $E/I$  ratio (*E/I imbalance*) due to reduced GABAergic inhibition combined with enhanced glutamatergic input was able to reproduce experimental data (Šišková et al., 2014; Table 5). We identified this configuration as a successful scenario 1 (green). In contrast, the configurations of increased *Excitation* and decreased *Inhibition* could not separately reproduce the data with low errors (Fig. 10D, left), although a decrease of GABAergic inhibition alone led to a shift in the preferred firing mode towards bursts (Fig. 10D, right), with a modestly increased firing rate. We observed in scenario 1 that the overall firing rate (Fig. 11A, left: WT  $3.35 \pm 1.87$  Hz, APP/PS1  $2.46 \pm 1.48$  Hz, P3 of APP/PS1 in scenario 1  $9.42 \pm 3.76$  Hz with  $P < 1 \times 10^{-4}$ ) and especially the number of bursts (Fig. 11A, middle: WT  $0.68 \pm 0.59$  Hz, APP/PS1  $0.52 \pm 0.52$  Hz, P3 of APP/PS1 in scenario 1  $1.98 \pm 0.65$  Hz with  $P < 1 \times 10^{-4}$ ) were significantly increased in the modified APP/PS1 cell group without affecting the single spike rate (Fig. 11A, middle: WT  $1.40 \pm 0.99$  Hz, APP/PS1  $1.09 \pm 0.56$  Hz, P3 of APP/PS1 in scenario 1  $1.67 \pm 0.98$  Hz) as reported in the experiments of Fig. 1B of Šišková et al. (2014). The rate of triplets for the parameter configuration P3 (Fig. 11A, right: WT  $0.23 \pm 0.34$  Hz, APP/PS1  $0.08 \pm 0.25$  Hz, P3 of APP/PS1 in scenario 1  $0.44 \pm 0.49$  Hz with  $P = 0.0964$  compared to WT) was not significantly higher but the trend was similar to data in Figs 1B and 2B of Šišková et al. (2014). It could be significantly increased with a simultaneous increase in single spike rate in the parameter configuration P4 (Fig. 11A: singlets  $2.07 \pm 1.11$  Hz with  $P = 0.0146$ , triplets  $0.5 \pm 0.44$  Hz with  $P = 0.0143$ ). Thus, given its successful replication of the transition to the bursting mode (Fig. 10D, right), scenario 1 with the parameter configuration P3 provides a good qualitative and a medium quantitative match with data.

**Scenario 2: increased extrinsic  $E/I$  ratio plus intrinsic ion channel alterations.** Ion channel alterations represent another potential mechanism of AD-associated neuronal hyperexcitability (Beck & Yaari, 2008; Garg et al., 2021; Ghatak et al., 2019; Liu et al., 2015; Niday & Bean, 2021; Wang et al., 2016; Wang, Kang et al., 2015; Wang, Zhang et al., 2015; Yaari et al., 2007; Zhang et al., 2014). Therefore, we have included changes in ion channel currents that have been reported in the literature. We performed targeted sensitivity analysis for the up- or down-scaling of four ion channel conductances known to play a role in AD-linked hyperexcitability (see Methods). Our simulation results confirmed the findings from previous experimental studies: we observed that by decreasing the  $I_{AHP}$  channel density and increasing

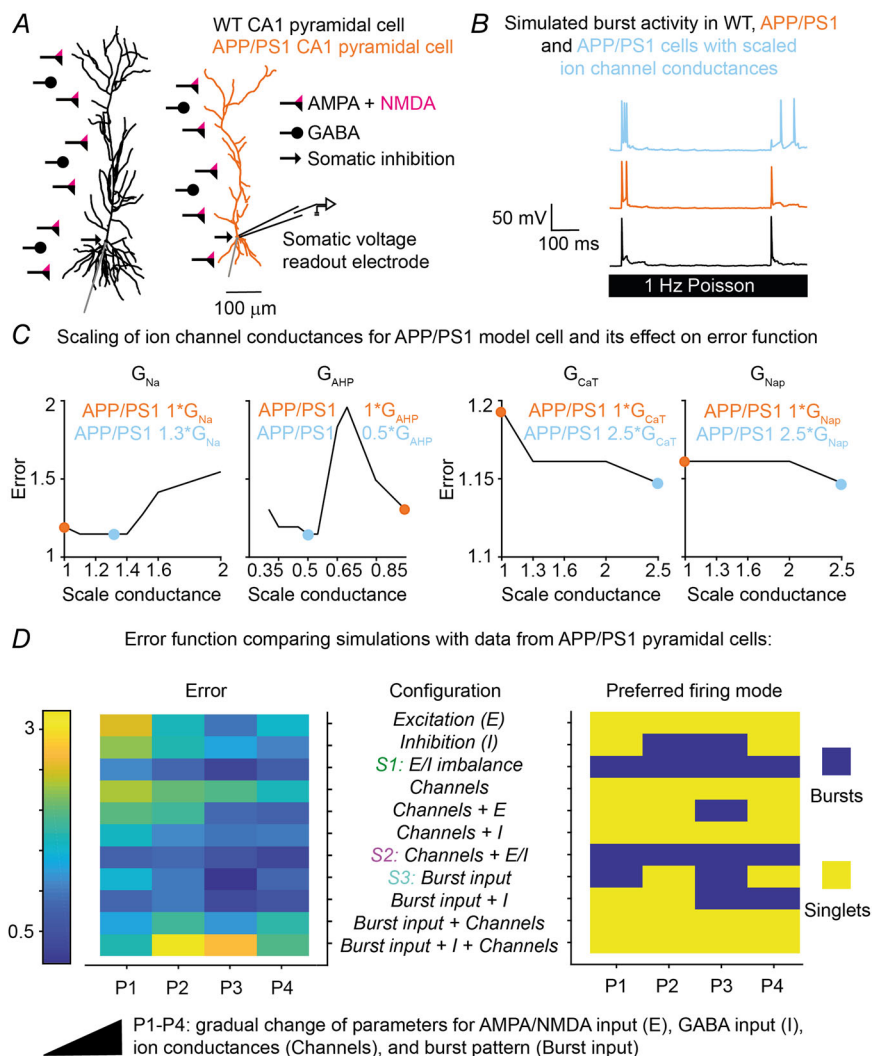
the density of  $I_{NaP}$ ,  $I_{Na}$  and  $I_{CaT}$  channels in sample APP/PS1 morphologies, the output firing rate and burst rate increased, leading to a minimum in the error function (Fig. 10C, marked with blue circles). Then we applied these changes to all APP/PS1 morphologies and scaled the four ion channel conductances accordingly (incremental scaling P1–P4 in the configuration *Channels* in Fig. 10D, left). This led to enhanced firing rates and burst rates, but not to a transition from solitary to burst firing, even when the conductances were scaled to extreme values (Fig. 10D, right). However, in combination with the change in  $E/I$  balance, the ion channel modifications were able to reproduce the experimental data (*Channels plus E/I* in Fig. 10D, compare Table 5). Therefore, we have identified this configuration as a successful scenario 2 (purple). Similarly as in scenario 1, also in scenario 2 the overall firing rate (Fig. 11B, left: WT  $3.35 \pm 1.87$  Hz, APP/PS1  $2.46 \pm 1.48$  Hz, P4 of APP/PS1 in scenario 2  $8.96 \pm 3.51$  Hz with  $P < 1 \times 10^{-4}$ ) and burst rate were

increased (Fig. 11B, middle: WT  $0.68 \pm 0.59$  Hz, APP/PS1  $0.52 \pm 0.52$  Hz, P4 of APP/PS1 in scenario 2  $1.88 \pm 0.63$  Hz with  $P < 1 \times 10^{-4}$ ). At the same time, in line with data from Šišková et al. (2014), the single spike rate remained similar (Fig. 11B, middle: WT  $1.40 \pm 0.99$  Hz, APP/PS1  $1.09 \pm 0.56$  Hz, P4 of APP/PS1 in scenario 2  $1.60 \pm 0.66$  Hz). Moreover, compared to the previous scenario 1, changes in the intrinsic excitability led to a significant boost in the triplet firing frequency (Fig. 11B, right: WT  $0.23 \pm 0.34$  Hz, APP/PS1  $0.08 \pm 0.25$  Hz, P4 of APP/PS1 in scenario 2  $0.56 \pm 0.60$  Hz with  $P = 0.0125$ ), which improved the quantitative match with electrophysiological data (Šišková et al., 2014 and Table 5).

**Scenario 3: increased excitatory network burst input.** CA1 PCs are embedded in a wider network with early-onset hyperexcitability (Kazim et al., 2021; Palop & Mucke, 2016; Selkoe, 2019; Zott et al., 2018). It has been shown that EC or CA3 hyperactivity can occur during

**Figure 10. Exploration of different configurations of AD-related extrinsic and intrinsic changes and their combinations that can lead to increased firing rates and bursting in APP/PS1 morphologies**

A, similar input organisation as Fig. 8A but with GABAergic inhibition extended to soma. B, example voltage traces in WT (black), APP/PS1 (orange) morphology and APP/PS1 morphology with altered ion channels (blue) during 1 Hz synaptic activation. C, error function (Eqns (1)–(3)) comparing firing rate data of Šišková et al. (2014) (see Table 5) with simulations of conductance changes for  $I_{Na}$ ,  $I_{AHP}$ ,  $I_{CaT}$  and  $I_{NaP}$  channels. The result of the original (WT) conductance value is shown in orange (scaled with 1) and the conductance with a smaller error in blue. D, matrix showing error function (left) and firing mode change (right) for 11 configurations (11 rows) of intrinsic and extrinsic parameter changes (middle) and four incremental changes in parameters (P1–P4 columns, details in Methods). Note that configurations S1, S2 and S3 provide both a good match with data (low error, left) and a successful transition to burst firing in APP/PS1 cells (right). Note also that isolated ion channel changes (C and 4th row in D) do not fully replicate data (see also Fig. 4A in Methods). [Colour figure can be viewed at [wileyonlinelibrary.com](http://wileyonlinelibrary.com)]



AD pathology (Angulo et al., 2017; Khan et al., 2013; Nuriel et al., 2017; Petrache et al., 2019) and possibly spread towards its postsynaptic CA1 area. Therefore, we tested whether increased network activity with enhanced bursting would transfer to increased burst firing in model neurons (configuration *Burst input* in Fig. 10D). Our investigations revealed that presynaptic input spike trains containing bursts (P3 in Fig. 11C, top) could evoke CA1 PC responses that were consistent with experimental data (Table 5). Therefore, we have selected this configuration as a successful scenario 3 (turquoise). The input pattern was sensitive as one less burst or one more singlet in the input spike train (P2 and P4 in Fig. 11C, top) failed to provide firing mode change towards bursts (Fig. 10D, right). We observed that changes in network activity in scenario 3 on average led to an increase of firing frequency in APP/PS1 cells, when compared to the behaviour of the

cell groups with a non-hyperexcitable (control) network input (Fig. 11C, left: WT  $4.74 \pm 2.08$  Hz, APP/PS1  $3.65 \pm 1.43$  Hz, P3 of APP/PS1 in scenario 3  $7.89 \pm 2.36$  Hz with  $P < 1 \times 10^{-4}$ ). This overall increase in the cell's excitability was due to a transition from solitary action potentials (1APs) to burst firing of more than one AP (Fig. 10D, right and Fig. 11C, middle: WT  $1.02 \pm 0.51$  Hz, APP/PS1  $0.83 \pm 0.48$  Hz, P3 of APP/PS1 in scenario 3  $1.99 \pm 0.69$  Hz with  $P < 1 \times 10^{-4}$ ). Particularly, in line with experimental data in Šišková et al. (2014), we observed a significant increase of the number of triplets (Fig. 11C, right: WT  $0.32 \pm 0.35$  Hz, APP/PS1  $0.38 \pm 0.32$  Hz, P3 of APP/PS1 in scenario 3  $0.79 \pm 0.62$  Hz with  $P = 3.64 \times 10^{-4}$ ), while the single AP firing rate remained constant (Fig. 11C, middle: WT  $1.66 \pm 0.68$  Hz, APP/PS1  $1.32 \pm 0.58$  Hz, P3 of APP/PS1 in scenario 3  $1.43 \pm 0.83$  Hz). This indicates a change of firing mode from predominantly single

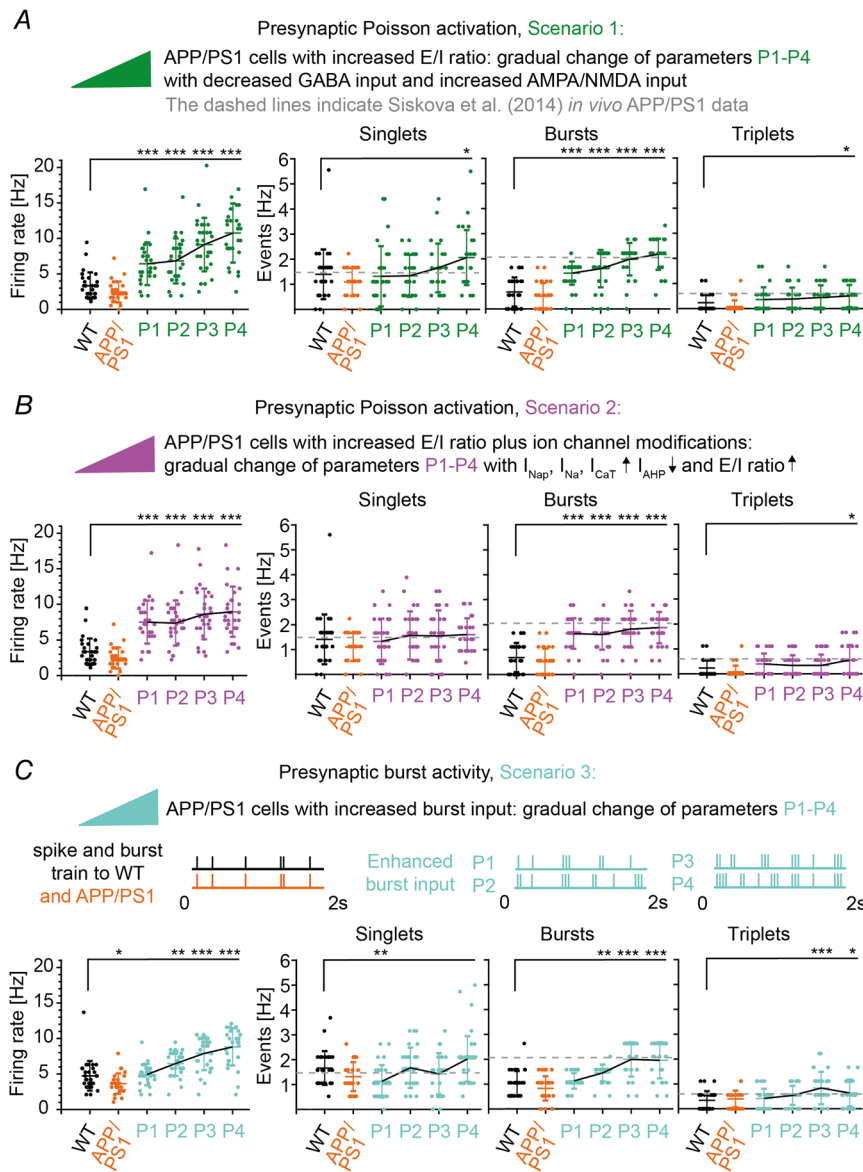


**Figure 11. Transition from solitary to burst firing in APP/PS1 cells due to gradual extrinsic (network) and concomitant intrinsic neuronal changes** A, scenario 1: left, overall firing rate in WT (black), APP/PS1 (orange) morphologies and in APP/PS1 morphologies with incrementally increased *E/I* ratio (green). Right, frequency of events for the same cell groups: single APs, bursts (>1 AP, ISI < 13.3 ms) and triplets (3 APs). B, scenario 2: left, overall firing rate in WT (black), APP/PS1 (orange) and APP/PS1 morphologies with incrementally increased *E/I* ratio as in scenario 2 (A) but additional, experimentally observed (Fig. 10C) ion channel changes (P1–P4, purple: increased  $I_{NaP}$ ,  $I_{Na}$ ,  $I_{CaT}$  densities, decreased  $I_{AHP}$  density; see details in Methods). Right, frequency of events for the same cell groups: single APs, bursts and triplets. C, scenario 3: left, overall firing rate in WT (black), APP/PS1 (orange) and APP/PS1 morphologies with incrementally increased burst input (P1–P4, turquoise). The exact input pattern of singlets, doublets, triplets and quadruplets can be seen above the panels. Right, frequency of events for the same cell groups: single APs, bursts and triplets. The dashed lines (grey) show the mean event rate according to Šišková et al. (2014). Throughout the figure, \* $P < 0.05$ , \*\* $P < 0.01$  and \*\*\* $P < 0.001$ . [Colour figure can be viewed at [wileyonlinelibrary.com](http://wileyonlinelibrary.com)]

spikes to burst firing in APP/PS1 cells with increased network activity input in scenario 3 ( $p_{1AP, > 1AP} = 0.00801$ ). Interestingly, bursty input in combination with reduced inhibition (*Burst input plus inhibition*) yielded comparable results to the ones observed for the bursts alone (Fig. 10D). This configuration can be seen as a particular version of *E/I imbalance* with the increased excitatory input due to bursts.

When we compare our results of network and ion channel changes, separately and in combination (Figs 10 and 11), we conclude that the output mode transition from solitary to burst firing that has been observed in APP/PS1 CA1 pyramidal neurons (Šišková et al., 2014) can be explained by changes in *E/I* balance (scenario 1), joint changes in *E/I* balance and ion channels (scenario 2), or modified input network dynamics (scenario 3).

## Discussion

In this study, we explored possible mechanisms accounting for the cellular and network hyperexcitability that has been observed in AD. We investigated the effect of dendritic degeneration, a hallmark of AD, on the cell's output behaviour. By using detailed compartmental models of CA1 pyramidal neurons based on 3D-reconstructed morphologies from WT and APP/PS1 mice, we showed that the dendritic structural changes in the APP/PS1 morphology group alone cannot explain the increased excitability observed in those cells experimentally. Interestingly, these results suggest that dendritic 'atrophy' could actually help maintain the cell's firing output to distributed synaptic inputs by compensating the loss of synapses through reducing the dendritic arbour and thereby increasing the input resistance. Moreover, when simulating clustered subregion-specific inputs, we observed that stronger degeneration in basal dendrites than apical dendrites leads by itself to decreased responsiveness of APP/PS1 cells to basal synaptic inputs but increased responsiveness to apical inputs. Functional consequences of such selective anatomical gating of layer-specific inputs (due to altered basal/apical dendrite ratio) are unclear. Enhanced responsiveness to apical synaptic activation might partially account for the enhanced firing in APP/PS1 CA1 PCs but cannot explain their enhanced bursting.

Since dendritic degeneration alone could not fully explain hyperexcitability observed in APP/PS1 mice, we consequently investigated potential alternative mechanisms leading to hyperexcitability in the animal model of AD. Our *in silico* analyses identified three scenarios that led to enhanced burst firing: (1) extrinsic changes in the form of enhanced excitation and reduced inhibition (altered *E/I* ratio), (2) combined extrinsic and intrinsic changes in the form of increased *E/I* ratio and

ion channel modifications, and (3) extrinsic changes in the form of increased network burst activity. Scenarios 1, 2 and 3 were not only able to explain increased neuronal firing rates but accounted also for the transition of the output mode from solitary to burst firing observed in APP/PS1 CA1 pyramidal neurons (Šišková et al., 2014).

## Dendritic degeneration and AD-related hyperexcitability

The basis of cellular hyperactivity in AD remains poorly understood. Several studies have investigated this phenomenon, either by using neuronal cultures and organoids (Ghatak et al., 2019) by *in vitro* (Šišková et al., 2014) and *in vivo* (Busche & Konnerth, 2016; Busche et al., 2008, 2012; Palop & Mucke, 2016; Palop et al., 2007; Šišková et al., 2014; Sosulina et al., 2021; Verret et al., 2012) approaches, or by using computational modelling (Šišková et al., 2014; van Elburg & van Ooyen, 2010; Vitale et al., 2021). Some of these studies suggested that the increased firing and bursting activity of the AD cells could be explained by neurite degeneration (Ghatak et al., 2019; Šišková et al., 2014) given that reduced dendritic length and complexity promotes the intrinsic excitability and integration of synaptic inputs (van Elburg & van Ooyen, 2010).

These proposals were based on the well-known electrotonic mechanisms (Van Ooyen et al., 2002) according to which dendritic degeneration reduces neuronal surface area and therefore decreases membrane conductance. This makes neurons more excitable in terms of larger voltage responses to somatic current injections as well as to synaptic stimulation (Šišková et al. 2014). In other words, a small cell with the same number of input synapses as a larger cell shows increased synaptic excitation. However, if also synaptic loss is considered then dendritic shortening with its increase in input resistance may counteract the lower number of synapses (Platschek et al., 2016). Although dendritic degeneration decreases the total number of synapses it keeps their relative number (synapse density per surface area) unchanged (Šišková et al. 2014). In this way, dendritic degeneration could paradoxically help maintain the size invariance of synaptically driven neuronal firing in the presence of rarefied synaptic input. This possibility has been previously shown in electrophysiological and morphological models of dendritic atrophy after entorhinal cortex lesion (Platschek et al., 2016). The models have revealed that dendritic atrophy was capable of adjusting the excitability of neurons, thus compensating for the denervation-evoked loss of synapses (Platschek et al., 2016, 2017). This computational principle has recently been generalised to all cell types

with a variety of dendritic shapes and sizes (Cuntz et al., 2021). Mathematical analysis and numerical simulations have shown that neuronal excitation in response to distributed inputs was largely unaffected by the dendrite length if synaptic density was kept constant (Cuntz et al., 2021).

Similarly, our detailed computational modelling here indicates that atrophied APP/PS1 cell morphologies probably do not lead on their own to increased firing and bursting as compared to the WT group, when driven by the same density of distributed synaptic inputs (Figs 7 and 8). The condition of the same synaptic density is based on similar spine density in APP/PS1 and WT dendrites (Šišková et al., 2014). Later stages of the AD progression (>20 months) show further spine loss and a decrease in spine density (Bittner et al., 2010; Knobloch & Mansuy, 2008; Spires-Jones et al., 2007).

Our results regarding excitability and dendritic degeneration remained consistent for both simple synaptic models with AMPA synapses (Fig. 7) and for more realistic and detailed synaptic models with distributed AMPA, NMDA and GABA-A synapses (Fig. 8B). This was not only true for changes in dendritic length in the APP/PS1 cell morphologies but also for other morphological measures such as the number of branch-points or the surface area of the cells (see Methods). In each case we found no hyperactivity in the APP/PS1 cells, which display dendritic degeneration. To test the robustness of our findings with respect to biophysical parameters, we implemented a second compartmental model by Jarsky et al. (2005), which confirmed the results of the model by Poirazi et al. (2003b) by showing no hyperexcitability in APP/PS1 cells due to purely morphological changes (see Methods).

We further investigated the effect of specific pathway inputs on the cell's response for both morphology groups and found a link between dendritic degeneration and change in excitability (Fig. 8). Stimulation of basal dendrites resulted in decreased firing of APP/PS1 cells compared to WT cells. Conversely, stimulation of apical dendrites increased the activity of APP/PS1 cells though it was only significant in the passive model (Fig. 8C and D, middle panels). This phenomenon is explained by a decrease in basal/apical ratio in APP/PS1 cells due to stronger basal degeneration resulting in less stimulated area per whole cell surface when only basal dendrites were activated. Vice versa, the stimulated area per whole cell surface was increased when only apical dendrites were activated (Fig. 9A, left). The different proportions of basal and apical dendrites therefore led to a selective gating of inputs from CA3. Interestingly, in case of equal basal/apical ratio this difference in excitation disappeared, as shown by the morphological modelling of artificially scaled WT and APP/PS1 cells in Fig. 9.

Taken together, our modelling indicates that additional, non-morphological changes are required to trigger increased burst firing in CA1 pyramidal neurons of APP/PS1 mice as reported in *in vivo* whole-cell and LFP recordings (Šišková et al., 2014). Our simulation results (Figs 7 and 8) show that the APP/PS1 cells display no hyperactivity compared to the WT cells even though they are on average smaller and have less synapses (see Methods). We therefore propose that dendritic atrophy might be a compensatory mechanism contributing to firing rate homeostasis (Platschek et al., 2016, 2017). The observation of morphological compensatory effects counteracting the functional impairments observed in AD have been repeatedly reported. Modifications such as an increase in size of remaining dendritic spines after AD-related spine loss (Dickstein et al., 2010; Fiala et al., 2002; Neuman et al., 2015) and changes in the topology and size of dendrites (Arendt et al., 1995; Graveland et al., 1985) seem to point towards the stabilising effect of spine and dendritic remodelling. Dendritic degeneration not only changes the overall size and complexity of the cell, but also the amount of membrane and available space for synaptic contacts. In fact, saving energy resources by reducing available surface membrane after synapse loss appears to be one of the reasons for dendritic retraction. Accordingly, dendritic retraction has been observed as a consequence of presynaptic neuron loss and an associated presynaptic denervation and synapse loss in AD but also other neuronal lesions (Platschek et al., 2017). However, the neuronal output is not necessarily decreased because the reduction in the number of synapses is well compensated morphologically by an increased input resistance (Cuntz et al., 2021; Platschek et al., 2016). In this way, dendritic changes that occur after the synapse loss observed in AD might help restore the input–output function of the cell. Such input–output homeostasis would be beneficial not only for the single neuron, but also for the network in which it is embedded. Similar compensatory strategies have been reported across species (Cuntz et al., 2013) and cell types (Platschek et al., 2016; Tripodi et al., 2008; Weaver & Wearne, 2008). In line with this idea, other studies have reported a conservation of the electrophysiological properties despite structural changes of AD-affected neurons (Rocher et al., 2008; Somogyi et al., 2016). Moreover, although it is commonly assumed that cells possess a specific structure in order to support a specific function, it has been recently shown that dendrite morphology can be well predicted by anatomical connectivity (Cuntz et al., 2010) and that the cell's size and shape is largely independent of its output under controlled conditions for distributed synaptic activation (Cuntz et al., 2021). This suggests that early AD-related modifications in the cellular structure (dendritic atrophy) compensate for synaptic loss as long as possible and keep the function intact.



### Alterations in extrinsic *E/I* balance and intrinsic ion channel properties

Since neuronal hyperexcitability in the APP/PS1 cells *in vivo* could not be accounted for by changes in the dendritic morphology, we explored possible alternative explanations for its origin. We investigated several observed configurations of extrinsic and intrinsic changes, namely elevated input frequency and correlation of excitatory input, diminished GABAergic inhibitory input, ion channel modifications, increased network burst activity, as well as combinations of these conditions.

First, *E/I* imbalance (scenario 1, Fig. 11A) in the form of increased input frequency and input correlations in excitatory connections (AMPA/NMDA) and decreased inhibitory synaptic activity could reproduce the data of Šišková et al. (2014) leading not only to elevated firing rates but also to an output mode switch from solitary to burst firing in APP/PS1 morphologies. Such alterations in *E/I* balance as a result of reduced inhibition and increased excitation have been shown previously in AD mouse models (Ambrad Giovannetti & Fuhrmann, 2019; Busche et al., 2008; Gervais et al., 2022; Palop & Mucke, 2016; Palop et al., 2007; Schmid et al., 2016; Xu et al., 2020; Hijazi et al., 2020; see also the recent review by Targa Dias Anastacio et al., 2022). Our computational study confirms that the experimentally observed dysfunction of GABAergic inhibition and the simultaneously enhanced glutamatergic excitation can be a major contributor to the AD-related hyperexcitability.

Second, the hyperexcitability in AD-affected brain cells has also been previously linked to ion channel modifications. In line with this, our simulations (Fig. 10C) showed several ion channel changes that increased the overall spike rate and burst firing: down-regulation of  $I_{\text{AHP}}$  current (Beck & Yaari, 2008; Niday & Bean, 2021; Wang, Zhang et al., 2015; Zhang et al., 2014), up-regulation of  $I_{\text{Na}}$  and persistent  $I_{\text{Nap}}$  currents (Beck & Yaari, 2008; Ghatak et al., 2019; Liu et al., 2015; Wang et al., 2016; Williams & Stuart, 1999; Yue et al., 2005) and up-regulation of T-type calcium current  $I_{\text{CaT}}$  (Beck & Yaari, 2008; Cain & Snutch, 2013; Garg et al., 2021; Medlock et al., 2018; Yaari et al., 2007). Our results suggest that intrinsic changes alone cannot explain the observed hyperexcitability since they did not reproduce the transition from single spiking to burst firing as reported in Šišková et al. (2014). Notably, we saw that joint alterations in *E/I* balance and ion channels together could replicate not only qualitatively but also quantitatively the AD-related hyperexcitability including the shift from single spikes to bursts of spikes (scenario 2, Fig. 11B). Our study therefore supports the idea that ion channel modifications during AD progression can contribute to the AD-related hyperexcitability. Especially, they can have a synergistic effect leading to more triplets than *E/I* imbalance alone and with a smaller parameter

shift away from the healthy control situation (e.g. in combination with a decrease in GABAergic inhibition). Interestingly, when we applied the same ion channel and network modifications to the WT morphologies we found an even higher increase in burst firing as compared to the APP/PS1 cells (see figures with control simulations in Methods). Thus, the AD-related dendritic degeneration can partially counter the increase in burst firing in APP/PS1 cells. This is in agreement with previous computational and morphological studies showing the effect of dendritic size and topology on the bursting behaviour of PCs (van Elburg & van Ooyen, 2010).

Third, previous studies have observed an increased network activity in AD-affected brain regions (Kazim et al., 2021; Maestú et al., 2021; Palop & Mucke, 2016; Šišková et al., 2014; Selkoe, 2019; Zott et al., 2018), which eventually can lead to epileptiform activity (Minkeviciene et al., 2009; Noebels, 2011). We found that increasing the excitability of the network by enhancing the excitatory input in the shape of bursts that were fed to our APP/PS1 CA1 pyramidal model cells can sufficiently boost their bursting frequency and alter the predominant mode of firing from single spike to burst firing (scenario 3, Fig. 11C) as observed in APP/PS1 mice (Šišková et al., 2014). Thus, our modelling predicts a significant contribution of extrinsic network bursts to target network hyperactivation. Such hyperactivity in AD-affected areas such as entorhinal cortex or CA3 (Angulo et al., 2017; Duffy et al., 2015; Khan et al., 2013; Nuriel et al., 2017; Petrache et al., 2019) can spread into the CA1 area and lead to a network-dependent increase in firing rate and burstiness. Since neurons are embedded in a network of other AD-affected neurons, this could lead to a cascade effect, amplifying the network hyperactivity. It would be interesting to apply information from theoretical analyses to such AD-related changes of spreading activity in hippocampal subregions as performed recently for synapse loss simulations (Świetlik et al., 2019).

In this study, we focused on stages of AD progression, at which amyloid plaques can be reliably observed. A recent study in transgenic rats has provided *in vivo* evidence that, at an early pre-plaque stage, CA1 hyperexcitability is mediated predominantly by increased intrinsic excitability (Sosulina et al., 2021). Accordingly, the dysfunction of inhibitory and excitatory transmission (Busche & Konnerth, 2016) would be expected to play a role at later stages of AD although the precise sequence of pathophysiological events remains to be established. It would be insightful to model earlier stages mechanistically and compare them to the later stages capturing not only the later-stage synergy of extrinsic and intrinsic pathomechanisms but also their initial sequence and dynamics in time. First steps towards such stage-dependent computational synthesis have been recently reported in a study of APP/PS1 mice at three

different ages (Vitale et al., 2021). This work revealed age-dependent changes in membrane time constant, expression of HCN channels, AP width and firing behaviour (evoked by somatic current injections) in APP/PS1 animals. Although measuring and modelling firing behaviour triggered by somatic current injections is important, our study shows that for a better understanding of age-dependent progress in AD-related hyperexcitability of single cells and networks, it will be important to characterise and model also the more natural, i.e. synaptically driven, firing behaviour.

### Limitations and applicability

There are additional mechanisms underlying AD-associated changes in extrinsic and intrinsic properties that we have not systematically tested in our simulations. For example, amyloid- $\beta$  accumulation as one of the hallmarks of AD progression may affect extracellular glutamate concentrations (Bao et al., 2021; Bezprozvanny & Mattson, 2008; Scimemi et al., 2013; Targa Dias Anastacio et al., 2022). Our simulations showed that indeed an increased NMDA time constant, which represented a delayed clearance of synaptically released glutamate, can result in an increased firing rate of APP/PS1 cells (see Fig. 4B in Methods). However, the burst firing rate remained unchanged with only the single AP firing rate being elevated indicating that other changes are necessary to fully explain hyperexcitability data. The impairment of synaptic plasticity due to amyloid- $\beta$  accumulation is a further indicator of AD leading to inhibited long-term potentiation and memory deficits (Rowan et al., 2003; Shankar et al., 2008). This impairment, however, may rather counteract the hyperexcitability observed in the APP/PS1 morphologies. Axon initial segment (AIS) properties are well known as an important factor for neuronal excitability (Evans et al., 2015; Kuba et al., 2014). Impaired AIS plasticity due to AD-related amyloid- $\beta$  proximity can therefore lead to alterations in the cellular excitability (Booker et al., 2020; Dongmin Sohn et al., 2019; León-Espinosa et al., 2012; Sun et al., 2014; Zhang et al., 2014). We did not include AIS changes in our study since we have no anatomical information for the examined morphologies. However, future work should investigate the role of the AIS and its potential changes in AD-related hyperactivity.

One caveat is that our work focused specifically on the AD-related hyperexcitability in the hippocampus of APP/PS1 mice. Hyperexcitability in other brain areas in these and other AD mice might be a result of other or additional circuit mechanisms. Indeed, a recent study has shown that early AD-related hyperexcitability in the somatosensory cortex of the familial AD mouse model is a consequence of a dysfunction in

the firing of GABAergic parvalbumin interneurons due to alterations of their potassium (Kv3) channels (Olah et al., 2022).

With respect to ion channel variability and degeneracy (Drion et al., 2015; Goillard & Marder, 2021; O'Leary, 2018; Schneider et al., 2021), it is likely that individual CA1 PCs react differently to AD with a variety of ion channel modifications that nevertheless can lead to the same neuronal hyperactivity with increased firing rates and burst rates. In addition, depending on the stage of the disease, different proportions of neurons may be affected by AD with a subset of them displaying hyperexcitability or hypoexcitability (Busche et al., 2008; Dunn & Kaczorowski, 2019; Zott et al., 2018) further affecting the variability in the network. In a healthy brain, the variability in ion channel expression and cellular excitability normally supports resilience (cf. Rich et al., 2022) and homeostasis. However, the homeostatic compensation might only be possible for a limited range of parameters or fail due to the complex interactions in the high-dimensional parameter space of the extrinsic and intrinsic neuronal mechanisms (O'Leary, 2018; Stöber et al., 2022; Yang et al., 2022). Even though the high-dimensional parameter space might offer more possible solutions for firing rate homeostasis (Schneider et al., 2021), these solutions might be difficult to find due to the necessary adjustment of several ion channels and/or extrinsic parameters for multiple properties at the same time (Yang et al., 2022; but see also Jedlicka et al., 2022). Indeed, the failure of homeostatic machinery including dysregulation of firing rate homeostasis is one of the main hypotheses for the vicious circle of AD progression (Dunn & Kaczorowski, 2019; Frere & Slutsky, 2018). Future modelling and experimental studies should address the variability in AD-related ion channel changes and in the failure of firing homeostasis.

Moreover, in our simulations we have implemented the same AD-linked parameter alterations (related to  $E/I$  imbalance and/or ion channel changes) in all AD morphologies. In reality it is possible that some neurons may be hyperexcitable entirely due to impaired  $E/I$  balance whereas other neurons may be hyperexcitable due to impaired  $E/I$  balance combined with ion channel alterations. The cell-to-cell heterogeneity of these effects may depend on the stage of AD progress.

### Multiple configurations of pathomechanisms leading to AD-related hyperexcitability

Our findings of several mechanisms involved in hyperexcitability in AD can be compared to the general and increasingly accepted concept of degeneracy (Edelman & Gally, 2001). In complex degenerate systems, such as the nervous system, multiple distinct mechanisms can

be sufficient, but typically no particular mechanism is necessary, to account for a given function or malfunction, such as normal excitability or hyperexcitability (Kamaleddin, 2022; see also Medlock et al., 2022; Neymotin et al., 2016; O'Leary, 2018; Ratté & Prescott, 2016). Our results suggest that alterations of extrinsic mechanisms are necessary while intrinsic ion channel changes can contribute to but are not necessary in AD hyperexcitability. Multiple extrinsic and intrinsic mechanisms together are sufficient to increase neuronal excitability in AD, but not a particular change of a single feature is necessary. More concretely, with respect to the altered spike pattern in AD mice (Šišková et al., 2014), we show that enhanced *E/I* ratio (scenario 1) or enhanced *E/I* ratio together with ion channel changes (scenario 2) or enhanced network burst input (scenario 3) are sufficient to account for the transition of output mode from solitary to burst firing.

Paradoxically, in systems displaying multi-causality and degeneracy, repairing a single target mechanism may not be enough for restoring their normal excitability (Kamaleddin, 2022; Stöber et al., 2022). Compensatory effects and adaptations (O'Leary, 2018) and their variability in different individuals (Medlock et al., 2022; Onasch & Gjorgjieva, 2020; Sakurai et al., 2014) can sometimes impede mono-causal therapeutic options targeting a single mechanism (Ratté & Prescott, 2016; Ratté et al., 2014). Therefore, multi-causal intervention strategies could include multiple sets of extrinsic and intrinsic perturbations potentially rescuing pathologically increased excitability in AD.

## References

- Adlard, P. A., & Vickers, J. C. (2002). Morphologically distinct plaque types differentially affect dendritic structure and organisation in the early and late states of Alzheimer's disease. *Acta Neuropathologica*, **103**(4), 377–383.
- Ambrad Giovannetti, E., & Fuhrmann, M. (2019). Unsupervised excitation: GABAergic dysfunctions in Alzheimer's disease. *Brain Research*, **1707**, 216–226.
- Anderton, B. H., Callahan, L., Coleman, P., Davies, P., Flood, D., Jicha, G. A., Ohm, T., & Weaver, C. (1998). Dendritic changes in Alzheimer's disease and factors that may underlie these changes. *Progress in Neurobiology*, **55**(6), 595–609.
- Anekonda, T. S., Quinn, J. F., Harris, C., Frahler, K., Wadsworth, T. L., & Woltjer, R. L. (2011). L-type voltage-gated calcium channel blockade with isradipine as a therapeutic strategy for Alzheimer's disease. *Neurobiology of Disease*, **41**(1), 62–70.
- Ang, C. W., Carlson, G. C., & Coulter, D. A. (2005). Hippocampal CA1 circuitry dynamically gates direct cortical inputs preferentially at theta frequencies. *Journal of Neuroscience*, **25**(42), 9567–9580.
- Angulo, S. L., Orman, R., Neymotin, S. A., Liu, L., Buitrago, L., Cepeda-Prado, E., Stefanov, D., Lytton, W. W., Stewart, M., Small, S. A., Duff, K. E., & Moreno, H. (2017). Tau and amyloid-related pathologies in the entorhinal cortex have divergent effects in the hippocampal circuit. *Neurobiology of Disease*, **108**, 261–276.
- Arellano, J. L., Benavides-Piccione, R., DeFelipe, J., & Yuste, R. (2007). Ultrastructure of dendritic spines: Correlation between synaptic and spine morphologies. *Frontiers in Neuroscience*, **1**(1), 131–143.
- Arendt, T., Brückner, M. K., Bigl, V., & Marcova, L. (1995). Dendritic reorganisation in the basal forebrain under degenerative conditions and its defects in Alzheimer's disease. III. The basal forebrain compared with other subcortical areas. *Journal of Comparative Neurology*, **351**(2), 223–246.
- Ascoli, G. A., Donohue, D. E., & Halavi, M. (2007). Neuro-morpho. org: a central resource for neuronal morphologies. *Journal of Neuroscience*, **27**(35), 9247–9251.
- Augustinack, J. C., Schneider, A., Mandelkow, E. M., & Hyman, B. T. (2002). Specific tau phosphorylation sites correlate with severity of neuronal cytopathology in Alzheimer's disease. *Acta Neuropathologica*, **103**(1), 26–35.
- Ballesteros-Yáñez, I., Benavides-Piccione, R., Elston, G. N., Yuste, R., & DeFelipe, J. (2006). Density and morphology of dendritic spines in mouse neocortex. *Neuroscience*, **138**(2), 403–409.
- Baloyannis, S. J. (2009). Dendritic pathology in Alzheimer's disease. *Journal of the Neurological Sciences*, **283**(1–2), 153–157.
- Bannister, N. J., & Larkman, A. U. (1995). Dendritic morphology of CA1 pyramidal neurons from the rat hippocampus: I. Branching patterns. *Journal of Comparative Neurology*, **360**(1), 150–160.
- Bao, Y., Yang, X., Fu, Y., Li, Z., Gong, R., & Lu, W. (2021). NMDAR-dependent somatic potentiation of synaptic inputs is correlated with  $\beta$  amyloid-mediated neuronal hyperactivity. *Translational Neurodegeneration*, **10**(1), 34.
- Beck, H., & Yaari, Y. (2008). Plasticity of intrinsic neuronal properties in CNS disorders. *Nature Reviews. Neuroscience*, **9**(5), 357–369.
- Beining, M., Mongiat, L. A., Schwarzacher, S. W., Cuntz, H., & Jedlicka, P. (2017). T2N as a new tool for robust electrophysiological modeling demonstrated for mature and adult-born dentate granule cells. *eLife*, **6**, e26517.
- Benavides-Piccione, R., Fernaud-Espinosa, I., Robles, V., Yuste, R., & Defelipe, J. (2013). Age-based comparison of human dendritic spine structure using complete three-dimensional reconstructions. *Cerebral Cortex*, **23**(8), 1798–1810.
- Benavides-Piccione, R., Regalado-Reyes, M., Fernaud-Espinosa, I., Kastanaukaite, A., Tapia-González, S., León-Espinosa, G., Rojo, C., Insausti, R., Segev, I., & Defelipe, J. (2020). Differential structure of hippocampal CA1 pyramidal neurons in the human and mouse. *Cerebral Cortex*, **30**, 730–752.
- Berridge, M. J. (2014). Calcium regulation of neural rhythms, memory and Alzheimer's disease. *Journal of Physiology*, **592**(2), 281–293.

- Bezchlibnyk, Y. B., Stone, S. S., Hamani, C., & Lozano, A. M. (2017). High frequency stimulation of the infralimbic cortex induces morphological changes in rat hippocampal neurons. *Brain Stimulation*, **10**(2), 315–323.
- Bezprozvanny, I., & Mattson, M. P. (2008). Neuronal calcium mishandling and the pathogenesis of Alzheimer's disease. *Trends in Neurosciences*, **31**(9), 454–463.
- Bittner, K. C., Andrasfalvy, B. K., & Magee, J. C. (2012). Ion channel gradients in the apical tuft region of CA1 pyramidal neurons. *PLoS One*, **7**(10), e46652.
- Bittner, T., Fuhrmann, M., Burgold, S., Ochs, S. M., Hoffmann, N., Mitteregger, G., Kretzschmar, H., Laferla, F. M., & Herms, J. (2010). Multiple events lead to dendritic spine loss in triple transgenic Alzheimer's disease mice. *PLoS One*, **5**(11), e15477.
- Bloss, E. B., Cembrowski, M. S., Karsh, B., Colonell, J., Fetter, R. D., & Spruston, N. (2016). Structured dendritic inhibition supports branch-selective integration in CA1 pyramidal cells. *Neuron*, **89**(5), 1016–1030.
- Bojarski, L., Herms, J., & Kuznicki, J. (2008). Calcium dysregulation in Alzheimer's disease. *Neurochemistry International*, **52**(4–5), 621–633.
- Booker, S. A., De Oliveira, L. S., Anstey, N. J., Kozic, Z., Dando, O. R., Jackson, A. D., Baxter, P. S., Isom, L. L., Sherman, D. L., Hardingham, G. E., Brophy, P. J., Wyllie, D. J. A., & Kind, P. C. (2020). Input-output relationship of ca1 pyramidal neurons reveals intact homeostatic mechanisms in a mouse model of fragile × syndrome. *Cell Reports*, **32**(6), 107988.
- Born, H. A., Kim, J. Y., Savjani, R. R., Das, P., Dabaghian, Y. A., Guo, Q., Yoo, J. W., Schuler, D. R., Cirrito, J. R., Zheng, H., Golde, T. E., Noebels, J. L., & Jankowsky, J. L. (2014). Genetic suppression of transgenic APP rescues hypersynchronous network activity in a mouse model of Alzheimer's disease. *Journal of Neuroscience*, **34**(11), 3826–3840.
- Borst, A., & Haag, J. (1996). The intrinsic electrophysiological characteristics of fly lobula plate tangential cells: I. Passive membrane properties. *Journal of Computational Neuroscience*, **3**(4), 313–336.
- Braak, H., & Braak, E. (1991). Neuropathological staging of Alzheimer-related changes. *Acta Neuropathologica*, **82**(4), 239–259.
- Braak, H., Braak, E., & Bohl, J. (1993). Staging of Alzheimer-related cortical destruction. *European Neurology*, **33**(6), 403–408.
- Bromer, C., Bartol, T. M., Bowden, J. B., Hubbard, D. D., Hanka, D. C., Gonzalez, P. V., Kuwajima, M., Mendenhall, J. M., Parker, P. H., Abraham, W. C., Sejnowski, T. J., & Harris, K. M. (2018). Long-term potentiation expands information content of hippocampal dentate gyrus synapses. *Proceedings of the National Academy of Sciences, USA*, **115**, E2410–E2418.
- Brown, J. T., Chin, J., Leiser, S. C., Pangalos, M. N., & Randall, A. D. (2011). Altered intrinsic neuronal excitability and reduced Na<sup>+</sup> currents in a mouse model of Alzheimer's disease. *Neurobiology of Aging*, **32**(11), 2109.e1–2109.e14.
- Busche, M., Eichhoff, G., Adelsberger, H., Abramowski, D., Wiederhold, K., Haass, C., Staufenbiel, M., Konnerth, A., & Garaschuk, O. (2008). Clusters of hyperactive neurons near amyloid plaques in a mouse model of Alzheimer's disease. *Science*, **321**(5896), 1686–1689.
- Busche, M. A., Chen, X., Henning, H. A., Reichwald, J., Staufenbiel, M., Sakmann, B., & Konnerth, A. (2012). Critical role of soluble amyloid- $\beta$  for early hippocampal hyperactivity in a mouse model of Alzheimer's disease. *Proceedings of the National Academy of Sciences, USA*, **109**(22), 8740–8745.
- Busche, M. A., Grienberger, C., Keskin, A. D., Song, B., Neumann, U., Staufenbiel, M., Förstl, H., & Konnerth, A. (2015). Decreased amyloid- $\beta$  and increased neuronal hyperactivity by immunotherapy in Alzheimer's models. *Nature Neuroscience*, **18**(12), 1725–1727.
- Busche, M. A., Kekuš, M., Adelsberger, H., Noda, T., Förstl, H., Nelken, I., & Konnerth, A. (2015). Rescue of long-range circuit dysfunction in Alzheimer's disease models. *Nature Neuroscience*, **18**(11), 1623–1630.
- Busche, M. A., & Konnerth, A. (2015). Neuronal hyperactivity – A key defect in Alzheimer's disease? *BioEssays*, **37**(6), 624–632.
- Busche, M. A., & Konnerth, A. (2016). Impairments of neural circuit function in Alzheimer's disease. *Philosophical Transactions of the Royal Society B: Biological Sciences*, **371**(1700), 20150429.
- Cain, S. M., & Snutch, T. P. (2013). T-type calcium channels in burst-firing, network synchrony, and epilepsy. *Biochimica et Biophysica Acta – Biomembranes*, **1828**(7), 1572–1578.
- Carnevale, N. T., Tsai, K. Y., Claiborne, B. J., & Brown, T. H. (1997). Comparative electrotonic analysis of three classes of rat hippocampal neurons. *Journal of Neurophysiology*, **78**(2), 703–720.
- Chen, C. (2005). beta-Amyloid increases dendritic Ca<sup>2+</sup> influx by inhibiting the A-type K<sup>+</sup> current in hippocampal CA1 pyramidal neurons. *Biochemical and Biophysical Research Communications*, **338**(4), 1913–1919.
- Cochran, J. N., Hall, A. M., & Roberson, E. D. (2014). The dendritic hypothesis for Alzheimer's disease pathophysiology. *Brain Research Bulletin*, **103**, 18–28.
- Craig, M. T., & McBain, C. J. (2015). Fast gamma oscillations are generated intrinsically in CA1 without the involvement of fast-spiking basket cells. *Journal of Neuroscience*, **35**(8), 3616–3624.
- Culmone, V., & Migliore, M. (2012). Progressive effect of beta amyloid peptides accumulation on CA1 pyramidal neurons: A model study suggesting possible treatments. *Frontiers in Computational Neuroscience*, **6**, 52.
- Cuntz, H., Bird, A. D., Mittag, M., Beining, M., Schneider, M., Mediavilla, L., Hoffmann, F. Z., Deller, T., & Jedlicka, P. (2021). A general principle of dendritic constancy: A neuron's size- and shape-invariant excitability. *Neuron*, **109**(22), 3647–3662.e7.
- Cuntz, H., Borst, A., & Segev, I. (2007). Optimization principles of dendritic structure. *Theoretical Biology and Medical Modelling*, **4**(1), 1–8.

- Cuntz, H., Forstner, F., Borst, A., & Häusser, M. (2010). One rule to grow them all: A general theory of neuronal branching and its practical application. *PLoS Computational Biology*, **6**(8), e1000877.
- Cuntz, H., Forstner, F., Borst, A., & Häusser, M. (2011). The TREES toolbox – Probing the basis of axonal and dendritic branching. *Neuroinformatics*, **9**(1), 91–96.
- Cuntz, H., Forstner, F., Schnell, B., Ammer, G., Raghu, S. V., & Borst, A. (2013). Preserving neural function under extreme scaling. *PLoS One*, **8**(8), e71540.
- Dhupia, N., Rathour, R. K., & Narayanan, R. (2015). Dendritic atrophy constricts functional maps in resonance and impedance properties of hippocampal model neurons. *Frontiers in Cellular Neuroscience*, **8**, 456.
- Dickerson, B. C., Salat, D. H., Greve, D. N., Chua, E. F., Rand-Giovannetti, E., Rentz, D. M., Bertram, L., Mullin, K., Tanzi, R. E., Blacker, D., Albert, M. S., & Sperling, R. A. (2005). Increased hippocampal activation in mild cognitive impairment compared to normal aging and AD. *Neurology*, **65**(3), 404–411.
- Dickstein, D. L., Brautigam, H., Stockton, S. D., Jr., Schmeidler, J., & Hof, P. R. (2010). Changes in dendritic complexity and spine morphology in transgenic mice expressing human wild-type tau. *Brain Structure and Function*, **214**(2–3), 161.
- Dongmin Sohn, P., Tzu-Ling Huang, C., Yan, R., Fan, L., Tracy, T. E., Camargo, C. M., Montgomery, K. M., Arhar, T., Mok, S. A., Freilich, R., Baik, J., He, M., Gong, S., Roberson, E. D., Karch, C. M., Gestwicki, J. E., Xu, K., Kosik, K. S., Gan, L., & Appel Alzheimer, R. (2019). Pathogenic tau impairs axon initial segment plasticity and excitability homeostasis. *Neuron*, **104**(3), 458–470.e5.
- Drion, G., O'Leary, T., & Marder, E. (2015). Ion channel degeneracy enables robust and tunable neuronal firing rates. *Proceedings of the National Academy of Sciences, USA*, **112**, E5361–E5370.
- Duffy, A. M., Morales-Corraliza, J., Bermudez-Hernandez, K. M., Schaner, M. J., Magagna-Poveda, A., Mathews, P. M., & Scharfman, H. E. (2015). Entorhinal cortical defects in Tg2576 mice are present as early as 2–4 months of age. *Neurobiology of Aging*, **36**(1), 134–148.
- Dunn, A. R., & Kaczorowski, C. C. (2019). Regulation of intrinsic excitability: Roles for learning and memory, aging and Alzheimer's disease, and genetic diversity. *Neurobiology of Learning and Memory*, **164**, 107069.
- Edelman, G. M., & Gally, J. A. (2001). Degeneracy and complexity in biological systems. *Proceedings of the National Academy of Sciences, USA*, **98**(24), 13763–13768.
- Evans, M. D., Dumitrescu, A. S., Kruijssen, D. L., Taylor, S. E., & Grubb, M. S. (2015). Rapid modulation of axon initial segment length influences repetitive spike firing. *Cell Reports*, **13**(6), 1233–1245.
- Falke, E., Nissanov, J., Mitchell, T. W., Bennett, D. A., Trojanowski, J. Q., & Arnold, S. E. (2003). Subicular dendritic arborization in Alzheimer's disease correlates with neurofibrillary tangle density. *American Journal of Pathology*, **163**(4), 1615–1621.
- Ferrao Santos, S., Pierrot, N., & Octave, J. N. (2010). Network excitability dysfunction in Alzheimer's disease: Insights from in vitro and in vivo models. *Reviews in the Neurosciences*, **21**(3), 153–171.
- Fiala, J. C., Spacek, J., & Harris, K. M. (2002). Dendritic spine pathology: Cause or consequence of neurological disorders? *Brain Research Reviews*, **39**(1), 29–54.
- Frazzini, V., Guarnieri, S., Bomba, M., Navarra, R., Morabito, C., Mariggiò, M. A., & Sensi, S. L. (2016). Altered Kv2.1 functioning promotes increased excitability in hippocampal neurons of an Alzheimer's disease mouse model. *Cell Death and Disease*, **7**(2), e2100–e2100.
- Frere, S., & Slutsky, I. (2018). Alzheimer's disease: From firing instability to homeostasis network collapse. *Neuron*, **97**(1), 32–58.
- Garg, J., Lakhani, A., & Dave, V. (2021). Effects of the involvement of calcium channels on neuronal hyperexcitability related to Alzheimer's disease: A computational model. *Neurophysiology*, **52**(5), 334–347.
- Gervais, É., Iloun, P., Martianova, E., Bessa, A. C. G., Rivest, S., & Topolnik, L. (2022). Structural analysis of the microglia–interneuron interactions in the CA1 hippocampal area of the APP/PS1 mouse model of Alzheimer's disease. *Journal of Comparative Neurology*, **530**(9), 1423–1437.
- Geula, C., Mesulam, M. M., Saroff, D. M., & Wu, C. K. (1998). Relationship between plaques, tangles, and loss of cortical cholinergic fibers in Alzheimer disease. *Journal of Neuro-pathology and Experimental Neurology*, **57**(1), 63–75.
- Ghatak, S., Dolatabadi, N., Trudler, D., Zhang, X., Wu, Y., Mohata, M., Ambasadhan, R., Talantova, M., & Lipton, S. A. (2019). Mechanisms of hyperexcitability in Alzheimer's disease hiPSC-derived neurons and cerebral organoids vs. isogenic control. *eLife*, **8**, e50333.
- Goillard, J. M., & Marder, E. (2021). Ion channel degeneracy, variability and covariation in neuron and circuit resilience. *Annual Review of Neuroscience*, **44**(1), 335–357.
- Golding, N. L., Mickus, T. J., Katz, Y., Kath, W. L., & Spruston, N. (2005). Factors mediating powerful voltage attenuation along CA1 pyramidal neuron dendrites. *The Journal of Physiology*, **568**(1), 69–82.
- Good, T. A., Smith, D., & Murphy, R. M. (1996). Beta-amyloid peptide blocks the fast-inactivating K<sup>+</sup> current in rat hippocampal neurons. *Biophysical Journal*, **70**(1), 296–304.
- Graveland, G. A., Williams, R. S., & DiFiglia, M. (1985). Evidence for degenerative and regenerative changes in neostriatal spiny neurons in Huntington's disease. *Science*, **227**(4688), 770–773.
- Grienberger, C., Rochefort, N. L., Adelsberger, H., Henning, H. A., Hill, D. N., Reichwald, J., Staufenbiel, M., & Konnerth, A. (2012). Staged decline of neuronal function in vivo in an animal model of Alzheimer's disease. *Nature Communications*, **3**(1), 774.
- Grutzendler, J., Helmin, K., Tsai, J., & Gan, W. B. (2007). Various dendritic abnormalities are associated with fibrillar amyloid deposits in Alzheimer's disease. *Annals of the New York Academy of Sciences*, **1097**(1), 30–39.

- Hall, A. M., Throesch, B. T., Buckingham, S. C., Markwardt, S. J., Peng, Y., Wang, Q., Hoffman, D. A., & Roberson, E. D. (2015). Tau-dependent Kv4.2 depletion and dendritic hyperexcitability in a mouse model of Alzheimer's disease. *Journal of Neuroscience*, **35**(15), 6221–6230.
- Häusser, M. (2001). Synaptic function: Dendritic democracy. *Current Biology*, **11**(1), R10–R12.
- Hijazi, S., Heistek, T. S., Scheltens, P., Neumann, U., Shimshek, D. R., Mansvelder, H. D., Smit, A. B., & van Kesteren, R. E. (2020). Early restoration of parvalbumin interneuron activity prevents memory loss and network hyperexcitability in a mouse model of Alzheimer's disease. *Molecular Psychiatry*, **25**(12), 3380–3398.
- Hines, M. L., & Carnevale, N. T. (2004). Discrete event simulation in the NEURON environment. *Neurocomputing*, **58–60**, 1117–1122.
- Hollnagel, J. O., Elzoheiry, S., Gorgas, K., Kins, S., Beretta, C. A., Kirsch, J., Kuhse, J., Kann, O., & Kiss, E. (2019). Early alterations in hippocampal perisomatic GABAergic synapses and network oscillations in a mouse model of Alzheimer's disease amyloidosis. *PLoS One*, **14**(1), e0209228.
- Horvath, A. A., Papp, A., Zsuffa, J., Szucs, A., Luckl, J., Radai, F., Nagy, F., Hidasi, Z., Csukly, G., Barcs, G., & Kamondi, A. (2021). Subclinical epileptiform activity accelerates the progression of alzheimer's disease: A long-term eeg study. *Clinical Neurophysiology*, **132**(8), 1982–1989.
- Jarsky, T., Roxin, A., Kath, W. L., & Spruston, N. (2005). Conditional dendritic spike propagation following distal synaptic activation of hippocampal CA1 pyramidal neurons. *Nature Neuroscience*, **8**(12), 1667–1676.
- Jedlicka, P., Bird, A. D., & Cuntz, H. (2022). Pareto optimality, economy–effectiveness trade-offs and ion channel degeneracy: Improving population modelling for single neurons. *Open Biology*, **12**(7), 220073.
- Kamaleddin, M. A. (2022). Degeneracy in the nervous system: from neuronal excitability to neural coding. *BioEssays*, **44**(1), 2100148.
- Katz, Y., Menon, V., Nicholson, D. A., Geinisman, Y., Kath, W. L., & Spruston, N. (2009). Synapse distribution suggests a two-stage model of dendritic integration in CA1 pyramidal neurons. *Neuron*, **63**(2), 171–177.
- Kazim, S. F., Chuang, S. C., Zhao, W., Wong, R. K., Bianchi, R., & Iqbal, K. (2017). Early-onset network hyperexcitability in presymptomatic Alzheimer's disease transgenic mice is suppressed by passive immunization with anti-human APP/A $\beta$  antibody and by mGluR5 blockade. *Frontiers in Aging Neuroscience*, **9**, 71.
- Kazim, S. F., Seo, J. H., Bianchi, R., Larson, C. S., Sharma, A., Wong, R. K., Gorbachev, K. Y., & Pereira, A. C. (2021). Neuronal network excitability in Alzheimer's disease: The puzzle of similar versus divergent roles of amyloid  $\beta$  and tau. *eNeuro*, **8**(2), ENEURO.0418–20.2020.
- Kellner, V., Menkes-Caspi, N., Beker, S., & Stern, E. A. (2014). Amyloid- $\beta$  alters ongoing neuronal activity and excitability in the frontal cortex. *Neurobiology of Aging*, **35**(9), 1982–1991.
- Kerrigan, T. L., Brown, J. T., & Randall, A. D. (2014). Characterization of altered intrinsic excitability in hippocampal CA1 pyramidal cells of the A $\beta$ -overproducing PDAPP mouse. *Neuropharmacology*, **79**, 515–524.
- Keskin, A. D., Kekuš, M., Adelsberger, H., Neumann, U., Shimshek, D. R., Song, B., Zott, B., Peng, T., Förstl, H., Staufenbiel, M., Nelken, I., Sakmann, B., Konnerth, A., & Busche, M. A. (2017). BACE inhibition-dependent repair of Alzheimer's pathophysiology. *Proceedings of the National Academy of Sciences, USA*, **114**(32), 8631–8636.
- Khan, U. A., Liu, L., Provenzano, F. A., Berman, D. E., Profaci, C. P., Sloan, R., Mayeux, R., Duff, K. E., & Small, S. A. (2013). Molecular drivers and cortical spread of lateral entorhinal cortex dysfunction in preclinical Alzheimer's disease. *Nature Neuroscience*, **17**(2), 304–311.
- Kim, D. Y., Carey, B. W., Wang, H., Ingano, L. A., Binshtok, A. M., Wertz, M. H., Pettingell, W. H., He, P., Lee, V. M., Woolf, C. J., & Kovacs, D. M. (2007). BACE1 regulates voltage-gated sodium channels and neuronal activity. *Nature Cell Biology*, **9**(7), 755–764.
- Kim, Y., Hsu, C. L., Cembrowski, M. S., Mensh, B. D., & Spruston, N. (2015). Dendritic sodium spikes are required for long-term potentiation at distal synapses on hippocampal pyramidal neurons. *eLife*, **4**, e06414.
- Knobloch, M., & Mansuy, I. M. (2008). Dendritic spine loss and synaptic alterations in Alzheimer's disease. *Molecular Neurobiology*, **37**(1), 73–82.
- Krueppel, R., Remy, S., & Beck, H. (2011). Dendritic integration in hippocampal dentate granule cells. *Neuron*, **71**(3), 512–528.
- Kuba, H., Adachi, R., & Ohmori, H. (2014). Activity-dependent and activity-independent development of the axon initial segment. *Journal of Neuroscience*, **34**(9), 3443–3453.
- Le, R., Cruz, L., Urbanc, B., Knowles, R. B., Hsiao-Ashe, K., Duff, K., Irizarry, M. C., Stanley, H. E., & Hyman, B. T. (2001). Plaque-induced abnormalities in neurite geometry in transgenic models of Alzheimer disease: Implications for neural system disruption. *Journal of Neuropathology and Experimental Neurology*, **60**(8), 753–758.
- León-Espinosa, G., DeFelipe, J., & Muñoz, A. (2012). Effects of Amyloid- $\beta$  plaque proximity on the axon initial segment of pyramidal cells. *Journal of Alzheimer's Disease*, **29**(4), 841–852.
- Liebscher, S., Keller, G. B., Goltstein, P. M., Bonhoeffer, T., & Hübener, M. (2016). Selective persistence of sensorimotor mismatch signals in visual cortex of behaving Alzheimer's disease mice. *Current Biology*, **26**(7), 956–964.
- Liu, C., Tan, F. C. K., Xiao, Z. C., & Dawe, G. S. (2015). Amyloid precursor protein enhances Nav1.6 sodium channel cell surface expression. *Journal of Biological Chemistry*, **290**(19), 12048–12057.
- López-Madrona, V. J., Canals, S., Hernández, M., & Joan D'alacant, S. (2021). Functional interactions between entorhinal cortical pathways modulate theta activity in the hippocampus. *Biology*, **10**, 692.

- Maestú, F., de Haan, W., Busche, M. A., & DeFelipe, J. (2021). Neuronal excitation/inhibition imbalance: Core element of a translational perspective on Alzheimer pathophysiology. *Ageing Research Reviews*, **69**, 101372.
- Magee, J. C., & Cook, E. P. (2000). Somatic EPSP amplitude is independent of synapse location in hippocampal pyramidal neurons. *Nature Neuroscience*, **3**(9), 895–903.
- Maier, F. C., Wehrl, H. F., Schmid, A. M., Mannheim, J. G., Wiehr, S., Lerdkrai, C., Calaminus, C., Stahlschmidt, A., Ye, L., Burnet, M., Stiller, D., Sabri, O., Reischl, G., Staufenbiel, M., Garaschuk, O., Jucker, M., & Pichler, B. J. (2014). Longitudinal PET-MRI reveals  $\beta$ -amyloid deposition and rCBF dynamics and connects vascular amyloidosis to quantitative loss of perfusion. *Nature Medicine*, **20**(12), 1485–1492.
- Manns, J. R., Zilli, E. A., Ong, K. C., Hasselmo, M. E., & Eichenbaum, H. (2007). Hippocampal CA1 spiking during encoding and retrieval: Relation to theta phase. *Neurobiology of Learning and Memory*, **87**(1), 9–20.
- Masliah, E., Mallory, M., Hansen, L., DeTeresa, R., Alford, M., & Terry, R. (1994). Synaptic and neuritic alterations during the progression of Alzheimer's disease. *Neuroscience Letters*, **174**(1), 67–72.
- McDougal, R. A., Morse, T. M., Carnevale, T., Marenco, L., Wang, R., Migliore, M., Miller, P. L., Shepherd, G. M., & Hines, M. L. (2017). Twenty years of ModelDB and beyond: Building essential modeling tools for the future of neuroscience. *Journal of Computational Neuroscience*, **42**(1), 1–10.
- Medlock, L., Sekiguchi, K., Hong, S., Dura-Bernal, S., Lytton, W. W., & Prescott, S. A. (2022). Multiscale computer model of the spinal dorsal horn reveals changes in network processing associated with chronic pain. *Journal of Neuroscience*, **42**(15), 3133–3149.
- Medlock, L., Shute, L., Fry, M., Standage, D., & Ferguson, A. V. (2018). Ionic mechanisms underlying tonic and burst firing behavior in subfornical organ neurons: A combined experimental and modeling study. *Journal of Neurophysiology*, **120**(5), 2269–2281.
- Megias, M., Emri, Z., Freund, T. F., & Gulyás, A. I. (2001). Total number and distribution of inhibitory and excitatory synapses on hippocampal CA1 pyramidal cells. *Neuroscience*, **102**(3), 527–540.
- Melgosa-Ecenarro, L., Doostdar, N., Radulescu, C. I., Jackson, J. S., & Barnes, S. J. (2022). Pinpointing the locus of GABAergic vulnerability in Alzheimer's disease. In *Seminars in cell & developmental biology*. Elsevier.
- Merino-Serrais, P., Benavides-Piccione, R., Blazquez-Llorca, L., Kastanauskaite, A., Rábano, A., Avila, J., & Defelipe, J. (2013). The influence of phospho-tau on dendritic spines of cortical pyramidal neurons in patients with Alzheimer's disease. *Brain*, **136**(6), 1913–1928.
- Minkeviciene, R., Rheims, S., Dobszay, M. B., Zilberter, M., Hartikainen, J., Fülöp, L., Penke, B., Zilberter, Y., Harkany, T., Pitkänen, A., & Tanila, H. (2009). Amyloid  $\beta$ -induced neuronal hyperexcitability triggers progressive epilepsy. *Journal of Neuroscience*, **29**(11), 3453–3462.
- Moolman, D. L., Vitolo, O. V., Vonsattel, J. P. G., & Shelanski, M. L. (2004). Dendrite and dendritic spine alterations in Alzheimer models. *Journal of Neurocytology*, **33**(3), 377–387.
- Morse, T. M., Carnevale, N. T., Mutalik, P. G., Migliore, M., & Shepherd, G. M. (2010). Abnormal excitability of oblique dendrites implicated in early Alzheimer's: A computational study. *Frontiers in Neural Circuits*, **4**, 16.
- Müller, L., Kirschstein, T., Köhling, R., Kuhla, A., & Teipel, S. (2021). Neuronal hyperexcitability in APPSWE/PS1dE9 mouse models of Alzheimer's disease. *Journal of Alzheimer's Disease*, **81**(3), 855–869.
- Musial, T. F., Molina-Campos, E., Bean, L. A., Ybarra, N., Borenstein, R., Russo, M. L., Buss, E. W., Justus, D., Neuman, K. M., Ayala, G. D., Mullen, S. A., Voskobiynyk, Y., Tulisiak, C. T., Fels, J. A., Corbett, N. J., Carballo, G., Kennedy, C. D., Popovic, J., Ramos-Franco, J., ... & Nicholson, D. A. (2018). Store depletion-induced h-channel plasticity rescues a channelopathy linked to Alzheimer's disease. *Neurobiology of Learning and Memory*, **154**, 141–157.
- Neuman, K. M., Molina-Campos, E., Musial, T. F., Price, A. L., Oh, K. J., Wolke, M. L., Buss, E. W., Scheff, S. W., Mufson, E. J., & Nicholson, D. A. (2015). Evidence for Alzheimer's disease-linked synapse loss and compensation in mouse and human hippocampal CA1 pyramidal neurons. *Brain Structure and Function*, **220**(6), 3143.
- Neymotin, S. A., Dura-Bernal, S., Lakatos, P., Sanger, T. D., & Lytton, W. W. (2016). Multitarget multi-scale simulation for pharmacological treatment of dystonia in motor cortex. *Frontiers in Pharmacology*, **7**, 157.
- Niday, Z., & Bean, B. P. (2021). BK channel regulation of afterpotentials and burst firing in cerebellar purkinje neurons. *Journal of Neuroscience*, **41**(13), 2854–2869.
- Noebels, J. (2011). A perfect storm: Converging paths of epilepsy and Alzheimer's dementia intersect in the hippocampal formation. *Epilepsia*, **52**, 39–46.
- Nuriel, T., Angulo, S. L., Khan, U., Ashok, A., Chen, Q., Figueroa, H. Y., Emrani, S., Liu, L., Herman, M., Barrett, G., Savage, V., Buitrago, L., Cepeda-Prado, E., Fung, C., Goldberg, E., Gross, S. S., Hussaini, S. A., Moreno, H., Small, S. A., & Duff, K. E. (2017). Neuronal hyperactivity due to loss of inhibitory tone in APOE4 mice lacking Alzheimer's disease-like pathology. *Nature Communications*, **8**(1), 1–14.
- Ohline, S. M., Liu, X., Ibrahim, M. F., Mockett, B. M., Empson, R. M., Abraham, W. C., Iremonger, K. J., & Jones, P. P. (2022). Altered membrane properties but unchanged intrinsic excitability and spontaneous postsynaptic currents in an aged APPSwe/PS1dE9 model of Alzheimer's disease. *Frontiers in Cellular Neuroscience*, **16**, 456.
- Okuhara, D. Y., & Beck, S. G. (1998). Corticosteroids influence the action potential firing pattern of hippocampal subfield CA3 pyramidal cells. *Neuroendocrinology*, **67**(1), 58–66.
- Olah, V. J., Goettemoeller, A. M., Rayaprolu, S., Dammer, E. B., Seyfried, N. T., Rangaraju, S., Dimid-schstein, J., & Rowan, M. J. (2022). Biophysical kv3 channel alterations dampen excitability of cortical pv interneurons and contribute to network hyperexcitability in early alzheimer's. *eLife*, **11**, e75316.
- O'Leary, T. (2018). Homeostasis, failure of homeostasis and degenerate ion channel regulation. *Current Opinion in Physiology*, **2**, 129–138.

- Onasch, S., & Gjorgjieva, J. (2020). Circuit stability to perturbations reveals hidden variability in the balance of intrinsic and synaptic conductances. *Journal of Neuroscience*, **40**(16), 3186–3202.
- Palop, J. J., Chin, J., Roberson, E. D., Wang, J., Thwin, M. T., Bien-Ly, N., Yoo, J., Ho, K. O., Yu, G. Q., Kreitzer, A., Finkbeiner, S., Noebels, J. L., & Mucke, L. (2007). Aberrant excitatory neuronal activity and compensatory remodeling of inhibitory hippocampal circuits in mouse models of Alzheimer's disease. *Neuron*, **55**(5), 697–711.
- Palop, J. J., & Mucke, L. (2009). Epilepsy and cognitive impairments in Alzheimer disease. *Archives of Neurology*, **66**(4), 435–440.
- Palop, J. J., & Mucke, L. (2016). Network abnormalities and interneuron dysfunction in Alzheimer disease. *Nature Reviews. Neuroscience*, **17**(12), 777–792.
- Petrache, A. L., Rajulawalla, A., Shi, A., Wetzell, A., Saito, T., Saido, T. C., Harvey, K., & Ali, A. B. (2019). Aberrant excitatory-inhibitory synaptic mechanisms in entorhinal cortex microcircuits during the pathogenesis of Alzheimer's disease. *Cerebral Cortex*, **29**(4), 1834–1850.
- Platschek, S., Cuntz, H., Deller, T., & Jedlicka, P. (2017). Lesion-induced dendritic remodeling as a new mechanism of homeostatic structural plasticity in the adult brain. *The Rewiring Brain*, 203–218.
- Platschek, S., Cuntz, H., Vuksic, M., Deller, T., & Jedlicka, P. (2016). A general homeostatic principle following lesion induced dendritic remodeling. *Acta Neuropathologica Communications*, **4**(1), 19.
- Poirazi, P., Brannon, T., & Mel, B. W. (2003a). Arithmetic of subthreshold synaptic summation in a model CA1 pyramidal cell. *Neuron*, **37**(6), 977–987.
- Poirazi, P., Brannon, T., & Mel, B. W. (2003b). Pyramidal neuron as two-layer neural network. *Neuron*, **37**(6), 989–999.
- Pothmann, L., Klos, C., Braganza, O., Schmidt, S., Horno, O., Memmesheimer, R. M., & Beck, H. (2019). Altered dynamics of canonical feedback inhibition predicts increased burst transmission in chronic epilepsy. *Journal of Neuroscience*, **39**(45), 8998–9012.
- Pouille, F., & Scanziani, M. (2004). Routing of spike series by dynamic circuits in the hippocampus. *Nature*, **429**(6993), 717–723.
- Pyapali, G. K., Sik, A., Penttonen, M., Buzsaki, G., & Turner, D. A. (1998). Dendritic properties of hippocampal CA1 pyramidal neurons in the rat: Intracellular staining in vivo and in vitro. *Journal of Comparative Neurology*, **391**(3), 335–352.
- Ranasinghe, K. G., Kudo, K., Hinkley, L., Beagle, A., Lerner, H., Mizuiri, D., Findlay, A., Miller, B. L., Kramer, J. H., Gorno-Tempini, M. L., Rabinovici, G. D., Rankin, K. P., Garcia, P. A., Kirsch, H. E., Vossel, K., & Nagarajan, S. S. (2022). Neuronal synchrony abnormalities associated with subclinical epileptiform activity in early-onset Alzheimer's disease. *Brain*, **145**(2), 744–753.
- Rathour, R. K., Malik, R., & Narayanan, R. (2016). Transient potassium channels augment degeneracy in hippocampal active dendritic spectral tuning. *Scientific Reports*, **6**(1), 24678.
- Ratté, S., & Prescott, S. A. (2016). Afferent hyperexcitability in neuropathic pain and the inconvenient truth about its degeneracy. *Current Opinion in Neurobiology*, **36**, 31–37.
- Ratté, S., Zhu, Y., Lee, K. Y., & Prescott, S. A. (2014). Criticality and degeneracy in injury-induced changes in primary afferent excitability and the implications for neuropathic pain. *eLife*, **3**, e02370.
- Rich, S., Chameh, H. M., Lefebvre, J., & Valiante, T. A. (2022). Loss of neuronal heterogeneity in epileptogenic human tissue impairs network resilience to sudden changes in synchrony. *Cell Reports*, **39**(8), 110863.
- Roberson, E. D., Halabisky, B., Yoo, J. W., Yao, J., Chin, J., Yan, F., Wu, T., Hamto, P., Devidze, N., Yu, G. Q., Palop, J. J., Noebels, J. L., & Mucke, L. (2011). Amyloid- $\beta$ /Fyn-induced synaptic, network, and cognitive impairments depend on tau levels in multiple mouse models of Alzheimer's disease. *Journal of Neuroscience*, **31**(2), 700–711.
- Rocher, A. B., Kinson, M. S., & Luebke, J. I. (2008). Significant structural but not physiological changes in cortical neurons of 12-month-old Tg2576 mice. *Neurobiology of Disease*, **32**(2), 309.
- Rodrigues, Y. E., Da, J., & Freitas, S. (2017). CA1 and CA3 pyramidal cell morphologies under Alzheimer's disease amyloid beta interaction. *BioRxiv*, 187476.
- Rowan, M. J., Klyubin, I., Cullen, W. K., & Anwyl, R. (2003). Synaptic plasticity in animal models of early Alzheimer's disease. *Philosophical Transactions of the Royal Society of London Series B: Biological Sciences*, **358**(1432), 821–828.
- Rudinskiy, N., Hawkes, J. M., Betensky, R. A., Eguchi, M., Yamaguchi, S., Spires-Jones, T. L., & Hyman, B. T. (2012). Orchestrated experience-driven arc responses are disrupted in a mouse model of Alzheimer's disease. *Nature Neuroscience*, **15**(10), 1422–1429.
- Ruiter, M., Herstel, L. J., & Wierenga, C. J. (2020). Reduction of dendritic inhibition in CA1 pyramidal neurons in amyloidosis models of early Alzheimer's disease. *Journal of Alzheimer's Disease*, **78**(3), 951–964.
- Sakurai, A., Tamvacakis, A. N., & Katz, P. S. (2014). Hidden synaptic differences in a neural circuit underlie differential behavioral susceptibility to a neural injury. *eLife*, **3**, e02598.
- Sanabria, E. R., Su, H., & Yaari, Y. (2001). Initiation of network bursts by  $\text{Ca}^{2+}$ -dependent intrinsic bursting in the rat pilocarpine model of temporal lobe epilepsy. *Journal of Physiology*, **532**(1), 205–216.
- Scala, F., Fusco, S., Ripoli, C., Piacentini, R., Li Puma, D. D., Spinelli, M., Laezza, F., Grassi, C., & D'Ascenzo, M. (2015). Intra-neuronal A $\beta$  accumulation induces hippocampal neuron hyperexcitability through A-type  $\text{K}^+$  current inhibition mediated by activation of caspases and GSK-3. *Neurobiology of Aging*, **36**(2), 886–900.
- Scheibel, A. B. (1979). The hippocampus: Organizational patterns in health and senescence. *Mechanisms of Ageing and Development*, **9**(1–2), 89–102.
- Schmid, L. C., Mittag, M., Poll, S., Steffen, J., Wagner, J., Geis, H. R., Schwarz, I., Schmidt, B., Schwarz, M. K., Remy, S., & Fuhrmann, M. (2016). Dysfunction of somatostatin-positive interneurons associated with memory deficits in an Alzheimer's disease model. *Neuron*, **92**(1), 114–125.



- Schneider, M., Gidon, A., Triesch, J., Jedlicka, P., & Cuntz, H. (2021). Biological complexity facilitates tuning of the neuronal parameter space. *BioRxiv*. <https://doi.org/10.1101/2021.05.04.442120>
- Scimemi, A., Meabon, J. S., Woltjer, R. L., Sullivan, J. M., Diamond, J. S., & Cook, D. G. (2013). Amyloid- $\beta$ -1-42 slows clearance of synaptically released glutamate by mislocalizing astrocytic GLT-1. *Annals of Internal Medicine*, **158**, 5312–5318.
- Selkoe, D. J. (2019). Early network dysfunction in Alzheimer's disease. *Science*, **365**(6453), 540–541.
- Shankar, G. M., Li, S., Mehta, T. H., Garcia-Munoz, A., Shepardson, N. E., Smith, I., Brett, F. M., Farrell, M. A., Rowan, M. J., Lemere, C. A., Regan, C. M., Walsh, D. M., Sabatini, B. L., & Selkoe, D. J. (2008). Amyloid- $\beta$  protein dimers isolated directly from Alzheimer's brains impair synaptic plasticity and memory. *Nature Medicine*, **14**(8), 837–842.
- Šišková, Z., Justus, D., Kaneko, H., Friedrichs, D., Henneberg, N., Beutel, T., Pitsch, J., Schoch, S., Becker, A., von der Kammer, H., & Remy, S. (2014). Dendritic structural degeneration is functionally linked to cellular hyperexcitability in a mouse model of Alzheimer's disease. *Neuron*, **84**(5), 1023–1033.
- Somogyi, A., Katonai, Z., Alpár, A., & Wolf, E. (2016). A novel form of compensation in the Tg2576 amyloid mouse model of Alzheimer's disease. *Frontiers in Cellular Neuroscience*, **10**, 152.
- Sosulina, L., Mittag, M., Geis, H., Hoffmann, K., Klyubin, I., Qi, Y., Steffen, J., Friedrichs, D., Henneberg, N., Fuhrmann, F., Justus, D., Keppler, K., Cuello, A. C., Rowan, M. J., Fuhrmann, M., & Remy, S. (2021). Hippocampal hyperactivity in a rat model of Alzheimer's disease. *Journal of Neurochemistry*, **157**(6), 2128–2144.
- Spires, T. L., & Hyman, B. T. (2004). Neuronal structure is altered by amyloid plaques. *Reviews in the Neurosciences*, **15**(4), 267–278.
- Spires-Jones, T. L., Meyer-Luehmann, M., Osetek, J. D., Jones, P. B., Stern, E. A., Bacskai, B. J., & Hyman, B. T. (2007). Impaired spine stability underlies plaque-related spine loss in an Alzheimer's disease mouse model. *The American Journal of Pathology*, **171**(4), 1304–1311.
- Stöber, T. M., Batulin, D., Triesch, J., Narayanan, R., & Jedlicka, P. (2022). Degeneracy in epilepsy: Multiple routes to hyperexcitable brain circuits and their repair. *arXiv*. 220609621.
- Strüber, M., Sauer, J. F., Jonas, P., & Bartos, M. (2017). Distance-dependent inhibition facilitates focality of gamma oscillations in the dentate gyrus. *Nature Communications*, **8**(1), 758.
- Sun, X., Wu, Y., Gu, M., Liu, Z., Ma, Y., Li, J., & Zhang, Y. (2014). Selective filtering defect at the axon initial segment in Alzheimer's disease mouse models. *Proceedings of the National Academy of Sciences, USA*, **111**(39), 14271–14276.
- Świetlik, D., Białowas, J., Moryś, J., & Kusiak, A. (2019). Computer model of synapse loss during an Alzheimer's disease-like pathology in hippocampal subregions DG, CA3 and CA1 – The way to chaos and information transfer. *Entropy*, **21**(4), 408.
- Takahashi, H., & Magee, J. C. (2009). Pathway interactions and synaptic plasticity in the dendritic tuft regions of CA1 pyramidal neurons. *Neuron*, **62**(1), 102–111.
- Takahashi, H., Brasnjevic, I., Rutten, B. P., Van Der Kolk, N., Perl, D. P., Bouras, C., Steinbusch, H. W., Schmitz, C., Hof, P. R., & Dickstein, D. L. (2010). Hippocampal interneuron loss in an APP/PS1 double mutant mouse and in Alzheimer's disease. *Brain Structure and Function*, **214**(2–3), 145–160.
- Tan, Y., Deng, Y., & Qing, H. (2012). Calcium channel blockers and Alzheimer's disease. *Neural Regeneration Research*, **7**, 137–140.
- Targa Dias Anastacio, H., Matosin, N., & Ooi, L. (2022). Neuronal hyperexcitability in Alzheimer's disease: What are the drivers behind this aberrant phenotype? *Translational Psychiatry*, **12**(1), 1–14.
- Terry, R. D., Masliah, E., Salmon, D. P., Butters, N., DeTeresa, R., Hill, R., Hansen, L. A., & Katzman, R. (1991). Physical basis of cognitive alterations in Alzheimer's disease: Synapse loss is the major correlate of cognitive impairment. *Annals of Neurology*, **30**(4), 572–580.
- Tononi, G., Sporns, O., & Edelman, G. M. (1999). Measures of degeneracy and redundancy in biological networks. *Proceedings of the National Academy of Sciences, USA*, **96**(6), 3257–3262.
- Tripathy, S. J., Burton, S. D., Geramita, M., Gerkin, R. C., & Urban, N. N. (2015). Brain-wide analysis of electrophysiological diversity yields novel categorization of mammalian neuron types. *Journal of Neurophysiology*, **113**(10), 3474–3489.
- Tripodi, M., Evers, J. F., Mauss, A., Bate, M., & Landgraf, M. (2008). Structural homeostasis: Compensatory adjustments of dendritic arbor geometry in response to variations of synaptic input. *PLoS Biology*, **6**(10), 2172–2187.
- Trommald, M., Jensen, V., & Andersen, P. (1995). Analysis of dendritic spines in rat CA1 pyramidal cells intracellularly filled with a fluorescent dye. *Journal of Comparative Neurology*, **353**(2), 260–274.
- Tsai, J., Grutzendler, J., Duff, K., & Gan, W. B. (2004). Fibrillar amyloid deposition leads to local synaptic abnormalities and breakage of neuronal branches. *Nature Neuroscience*, **7**(11), 1181–1183.
- van Elburg, R. A., & van Ooyen, A. (2010). Impact of dendritic size and dendritic topology on burst firing in pyramidal cells. *PLoS Computational Biology*, **6**(5), 1–19.
- Van Ooyen, A., Duijnhouwer, J., Remme, M. W., & van Pelt, J. (2002). The effect of dendritic topology on firing patterns in model neurons. *Network: Computation in Neural Systems*, **13**(3), 311.
- Verret, L., Mann, E. O., Hang, G. B., Barth, A. M., Cobos, I., Ho, K., Devidze, N., Masliah, E., Kreitzer, A. C., Mody, I., Mucke, L., & Palop, J. J. (2012). Inhibitory interneuron deficit links altered network activity and cognitive dysfunction in Alzheimer model. *Cell*, **149**(3), 708–721.
- Vitale, P., Salgueiro-Pereira, A. R., Lupascu, C. A., Willem, M., Migliore, R., Migliore, M., & Marie, H. (2021). Analysis of age-dependent alterations in excitability properties of CA1 pyramidal neurons in an APPPS1 model of Alzheimer's disease. *Frontiers in Aging Neuroscience*, **13**, 1–15.

- Vossel, K., Ranasinghe, K. G., Beagle, A. J., La, A., Ah Pook, K., Castro, M., Mizuiri, D., Honma, S. M., Venkateswaran, N., Koestler, M., Zhang, W., Mucke, L., Howell, M. J., Possin, K. L., Kramer, J. H., Boxer, A. L., Miller, B. L., Nagarajan, S. S., & Kirsch, H. E. (2021). Effect of levetiracetam on cognition in patients with Alzheimer disease with and without epileptiform activity: A randomized clinical trial. *JAMA Neurology*, **78**(11), 1345–1354.
- Vossel, K. A., Beagle, A. J., Rabinovici, G. D., Shu, H., Lee, S. E., Naasan, G., Hegde, M., Cornes, S. B., Henry, M. L., Nelson, A. B., Seeley, W. W., Geschwind, M. D., Gorno-Tempini, M. L., Shih, T., Kirsch, H. E., Garcia, P. A., Miller, B. L., & Mucke, L. (2013). Seizures and epileptiform activity in the early stages of Alzheimer disease. *JAMA Neurology*, **70**(9), 1158–1166.
- Vossel, K. A., Ranasinghe, K. G., Beagle, A. J., Mizuiri, D., Honma, S. M., Dowling, A. F., Darwish, S. M., Van Berlo, V., Barnes, D. E., Mantle, M., Karydas, A. M., Coppola, G., Roberson, E. D., Miller, B. L., Garcia, P. A., Kirsch, H. E., Mucke, L., & Nagarajan, S. S. (2016). Incidence and impact of subclinical epileptiform activity in Alzheimer's disease. *Annals of Neurology*, **80**(6), 858–870.
- Vossel, K. A., Tartaglia, M. C., Nygaard, H. B., Zeman, A. Z., & Miller, B. L. (2017). Epileptic activity in Alzheimer's disease: Causes and clinical relevance. *The Lancet Neurology*, **16**(4), 311–322.
- Vyas, Y., Montgomery, J. M., & Cheyne, J. E. (2020). Hippocampal deficits in amyloid- $\beta$ -related rodent models of Alzheimer's disease. *Frontiers in Neuroscience*, **14**, 266.
- Wang, F., Zhang, Y., Wang, L., Sun, P., Luo, X., Ishigaki, Y., Sugai, T., Yamamoto, R., & Kato, N. (2015). Improvement of spatial learning by facilitating large-conductance calcium-activated potassium channel with transcranial magnetic stimulation in Alzheimer's disease model mice. *Neuropharmacology*, **97**, 210–219.
- Wang, L., Kang, H., Li, Y., Shui, Y., Yamamoto, R., Sugai, T., & Kato, N. (2015). Cognitive recovery by chronic activation of the large-conductance calcium-activated potassium channel in a mouse model of Alzheimer's disease. *Neuropharmacology*, **92**, 8–15.
- Wang, X., Zhang, X. G., Zhou, T. T., Li, N., Jang, C. Y., Xiao, Z. C., Ma, Q. H., & Li, S. (2016). Elevated neuronal excitability due to modulation of the voltage-gated sodium channel Nav1.6 by A $\beta$ 1–42. *Frontiers in Neuroscience*, **10**, 1–9.
- Weaver, C. M., & Wearne, S. L. (2008). Neuronal firing sensitivity to morphologic and active membrane parameters. *PLoS Computational Biology*, **4**(1), 130–150.
- Wellmer, J., Su, H., Beck, H., & Yaari, Y. (2002). Long-lasting modification of intrinsic discharge properties in subicular neurons following status epilepticus. *European Journal of Neuroscience*, **16**(2), 259–266.
- Williams, S. R., & Stuart, G. J. (1999). Mechanisms and consequences of action potential burst firing in rat neocortical pyramidal neurons. *The Journal of Physiology*, **521**(Pt 2), 467–482.
- Xu, W., Fitzgerald, S., Nixon, R. A., Levy, E., & Wilson, D. A. (2015). Early hyperactivity in lateral entorhinal cortex is associated with elevated levels of A $\beta$ PP metabolites in the Tg2576 mouse model of Alzheimer's disease. *Experimental Neurology*, **264**, 82–91.
- Xu, Y., Zhao, M., Han, Y., & Zhang, H. (2020). GABAergic inhibitory interneuron deficits in Alzheimer's disease: Implications for treatment. *Frontiers in Neuroscience*, **14**, 660.
- Yaari, Y., Yue, C., & Su, H. (2007). Recruitment of apical dendritic T-type Ca<sup>2+</sup> channels by back-propagating spikes underlies de novo intrinsic bursting in hippocampal epileptogenesis. *The Journal of Physiology*, **580**(2), 435.
- Yang, J., Shakil, H., Ratté, S., & Prescott, S. A. (2022). Minimal requirements for a neuron to coregulate many properties and the implications for ion channel correlations and robustness. *eLife*, **11**, e72875.
- Yue, C., Remy, S., Su, H., Beck, H., & Yaari, Y. (2005). Proximal persistent Na<sup>+</sup> channels drive spike after-depolarizations and associated bursting in adult CA1 pyramidal cells. *Journal of Neuroscience*, **25**(42), 9704–9720.
- Zhang, Y., Shi, Z. G., Wang, Z. H., Li, J. G., Chen, J. Y., & Zhang, C. (2014). Effects of amyloid  $\beta$ -peptide fragment 31–35 on the BK channel-mediated K<sup>+</sup> current and intracellular free Ca<sup>2+</sup> concentration of hippocampal CA1 neurons. *Neuroscience Letters*, **568**, 72–76.
- Zott, B., Busche, M. A., Sperling, R. A., & Konnerth, A. (2018). What happens with the circuit in Alzheimer's disease in mice and humans? *Annual Review of Neuroscience*, **41**(1), 277–297.
- Zott, B., Simon, M. M., Hong, W., Unger, F., Chen-Engerer, H. J., Frosch, M. P., Sakmann, B., Walsh, D. M., & Konnerth, A. (2019). A vicious cycle of  $\beta$  amyloid-dependent neuronal hyperactivation. *Science*, **365**(6453), 559–565.

## Additional information

### Data availability statement

The code and data for all figures are available at <https://zenodo.org/record/7583939>.

### Competing interests

The authors declare to have no competing financial interests.

### Author contributions

M.M., L.M., S.R., H.C. and P.J. designed the study. M.M. and L.M. performed the simulations and analysed the data. M.M., L.M., S.R., H.C. and P.J. wrote the paper. All authors approved the final version of the manuscript and agree to be accountable for all aspects of the work in ensuring that questions related to the accuracy or integrity of any part of the work are appropriately investigated and resolved.

## Funding

This work was supported by BMBF (No. 01GQ1406 – Bernstein Award 2013 to H.C., No. 031L0229, to P.J.), by University Medical Centre Giessen and Marburg (UKGM; to P.J.), by funds from the von Behring Rontgen Foundation (to P.J.) and by DFG SFB 1436 (to S.R.).

## Acknowledgements

We thank Claudia Kernberger for her help with the design of the graphical abstract.

Open access funding enabled and organized by Projekt DEAL.

## Keywords

degeneracy, dendritic constancy, hippocampus, morphological modelling, multi-causal pathogenesis

## Supporting information

Additional supporting information can be found online in the Supporting Information section at the end of the HTML view of the article. Supporting information files available:

## Statistical Summary Document

## Peer Review History